

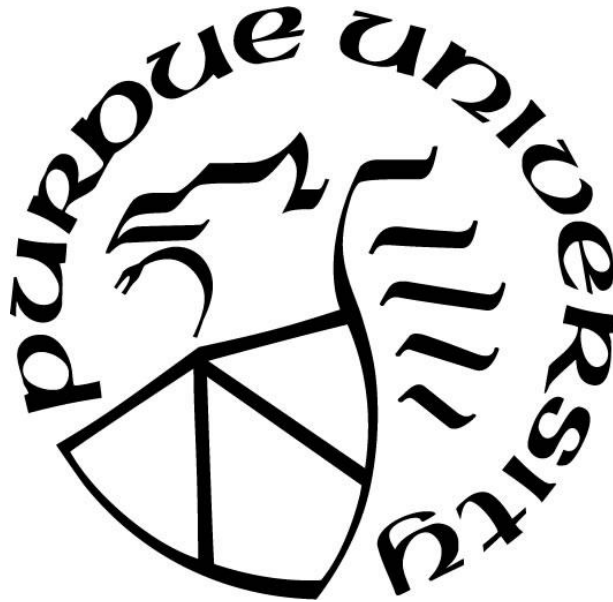
**MICROSTRUCTURE DEVELOPMENT IN MULTI-PASS LASER
MELTING OF AISI 8620 STEEL**

by
Matthew Binkley

A Thesis

*Submitted to the Faculty of Purdue University
In Partial Fulfillment of the Requirements for the degree of*

Master of Science in Materials Engineering



School of Materials Engineering

West Lafayette, Indiana

August 2020

**THE PURDUE UNIVERSITY GRADUATE SCHOOL
STATEMENT OF COMMITTEE APPROVAL**

Dr. Matthew Krane, Co-Chair
School of Materials Engineering

Dr. Kevin Trumble, Co-Chair
School of Materials Engineering

Dr. David Johnson
School of Materials Engineering

Dr. Michael Titus
School of Materials Engineering

Approved by:

Dr. David Bahr

This work is dedicated to my family

ACKNOWLEDGEMENTS

I would like to thank my family, friends, and colleagues for their support, guidance, and patience throughout this process. First, I would like to thank my advisors, Dr. Matthew J.M. Krane and Dr. Kevin Trumble who mentored me throughout my academic and professional development. I am forever grateful for their support and guidance in pursuing this work. Second, I would like to thank John Coleman for his patience and willingness to help progress and guide my understanding of numerical methods and coding used to create this work. This work would not have been possible without him. Finally, I would like to thank my mother, Teresa, and my father, Rob, for their endless love, support, and belief in me.

I would like to thank OakRidge National Lab, especially, Alex Plotkowsi and Keith Carver for their help in making the experiments performed in this work possible.

The funding of this research by Rolls-Royce Indianapolis is gratefully acknowledged.

TABLE OF CONTENTS

TABLE OF CONTENTS.....	5
LIST OF TABLES	7
LIST OF FIGURES	8
ABSTRACT.....	11
1. INTRODUCTION	12
1.1. Background	15
1.2. Initial Investigations into AM	22
1.3. Mechanical and microstructural property analysis.....	27
1.4. Overview	29
2. EXPERIMENTAL STUDY OF LASER MELTING.....	31
2.1. Choice of process parameters.....	31
2.1. Sample Preparation	33
2.2. Choice of Build Parameters	34
2.3. Results	36
2.3.1. Preliminary metallography with Nital and Picral etchants	36
2.3.2. Single Line Experiments.....	38
2.3.1. Multipass experiments	41
2.3.2. Other features of interest.....	46
2.3.3. Summary.....	48
3. MODEL	50
3.1. Analytical and Thermal Models.....	50
3.2. Numerical Model.....	55
3.2.1. Diffusional Transformation (JMAK).....	59

3.2.2.	Martensite Formation.....	61
3.2.3.	Austenitization and Tempering.....	62
3.2.4.	Hardness Calculation	64
3.2.5.	Fitting surface tension gradient.....	65
3.2.6.	Single Pass	67
3.2.7.	Multi-Pass	71
4.	SUMMARY AND FUTURE WORK	73
	REFERENCES	74

LIST OF TABLES

Table 1: AM steels and etchants used.....	29
Table 2: Parameters for Powder Bed Fusion AM for steels found in literature	32
Table 3: Composition of AISI 8620.[65].....	34
Table 4: Processing parameters for the six chosen speeds and powers to be put on the three pucks	35
Table 5: Average Vickers hardness measurements of single pass test cases taken at HV0.5 with one indent in each single pass for a total of 3 indents. The variation is the standard deviation of the indents. *400mm/sec/125W was taken at HV0.2 due to the size of the melt pools being so much smaller.....	40
Table 6: Hardness of multi-pass regions taken with HV0.2. Each section was indented 5 times and variation shown is the standard deviation. Note that in the 200 mm/sec/195W case each melt pool had such a large area of effect there was no difference between zones and the 400mm/sec/125W case had so little interaction between melt pools it was impossible to take measurements.	45
Table 7: Thermophysical properties of AISI 8620.[73].....	57
Table 8: Properties that required experimental calibration.....	57
Table 9: Compiled dimensions and hardness predictions of single pass cases.....	69
Table 10: Maximum hardness predicted for each multi-pass case.	72

LIST OF FIGURES

Figure 1: Graphic of powder bed fusion metal additive laser process.[15].....	14
Figure 2: Graphic of DED blown powder laser additive manufacturing process.[15]	15
Figure 3: Visualization of surface tension gradient on the melt pool fluid flow.	18
Figure 4: Schematic of laser hardening, showing the hardened zone (HZ) and the adjacent heat affected zone (HAZ).	21
Figure 5: Schematic of two pass laser hardening showing the overlap of the second pass onto the first where retransformation occurs and tempered region.	21
Figure 6: Process window for SM Raynor Ti-6Al-4V powder. Section I is the fully dense regime, II the over melting, and III the incomplete melting regimes[35].....	22
Figure 7: Illustration of laser passing through a powder bed showing the plume(gray) of microscopic sized particles and macroscopic ejecta(yellow).[13].....	24
Figure 8: Jominy end quench hardness results across a time-temperature-transformation diagram for AISI 8620.[49]	28
Figure 9: Finished sample pucks ground to the same height and grit blasted taken using cellphone camera.	34
Figure 10: Visual of the layout of the hatch region and laser passes on the top surface of the puck(a). Stereoscope top-down image of completed hatch and one single line test case as processed(b).	35
Figure 11: SEM images of multi-pass experiments etched with nital (a) and picral (b) processed at 200 mm/sec and 125 W.....	37
Figure 12: Picral etched SEM secondary images of the weld and surrounding microstructure for the single line laser welds, over ranges of power and velocity.....	39
Figure 13: Nanohardness map of single pass 200 mm/sec 125W case. Each tick represents 15 μm for a test space of 180x150 μm	41

Figure 14: Secondary SEM images of the multi-pass laser welds of the parameters of interest etched with picral showcasing the melt pools and heat treatment of previous passes. The laser alternates between into and out of the page progressing from the left to the right..... 42

Figure 15: Cartoon graphic of the multipass experiments with labeled regions for simplicity in discussion..... 43

Figure 16: Secondary SEM image of a zoomed in view of the tempered boundary showing increase in carbide amount in the 300 mm/sec 150 W case. The carbides are the white areas where carbon has migrated from the surrounding martensite and come out of solution..... 44

Figure 17: Nano-hardness of the multi-pass region. Melt pool lines are approximated by the dashed lines. The tempered region is shown(A)..... 46

Figure 18: Single pass where variations outside the melt line are clearly visible. Closeup region is outlined in black square. 47

Figure 19: Close-up of features outside melt pool showing partial transformation of pearlite with minimal impact to ferrite. 48

Figure 20: Coordinate system of Rosenthal’s solution as it moves with the heat source.[72] 51

Figure 21: Graphical solutions of the Rosenthal equation across all planes: the z-plane(a), (x-plane(b), and the y-plane(c). Parameters used were 0.4m/s and 195 W..... 52

Figure 22: Rosenthal’s equation plus conduction for 2 laser passes at 0.4m/sec, 195W, and 100 μm spacing..... 53

Figure 23: Time versus Temperature plots for a single pass of 400mm/sec and 195W in the Numerical Model. The distances of the legend are μm steps away from the center of the melt pool where probes were placed in the y-direction. 54

Figure 24: Time versus Temperature plots for multiple passes of 400mm/sec and 195W in the Numerical Model. The distances of the legend are μm steps away from the center of the melt pool where probes were placed in the y-direction. 55

Figure 25: Model weld lines overlaid on experimental weld lines in red. In case of double line, the outer red line is the full melt pool..... 58

Figure 26: Calculation of anisothermal incubation time found by using Scheil's additivity principle.[77].....	60
Figure 27: Visualization of anisothermal growth kinetics using the JMAK equation coupled with Scheil's additivity principle.[76]	61
Figure 28: Statistical distribution of I_x transformation. The dashed line showing phase transformed at the individual time and the solid showing cumulative transformation.....	63
Figure 29: Linear approximation of f_x allowing for model simplicity.....	64
Figure 30: Overlay of modeled melt pool size in outer red line for different values of surface tension gradient overlaid in red on experimental case 400mm/sec 125W.....	67
Figure 31: Single Pass no flow model cases depicting hardness.....	68
Figure 32: Single pass flow model cases depicting hardness.	69
Figure 33: Predicted martensite fraction of single pass weld pools with flow with size of the melt pool overlaid as the larger radial white contour.....	70
Figure 34:Hardness prediction overlaid on experimental case for 400mm/sec 125W.	71
Figure 35: Predicted hardness profiles of multi-pass cases.	72

ABSTRACT

An existing thermal model for laser melting and additive manufacturing (AM) was expanded to include phase transformation and hardness predictions for an alloy steel and coupled to experimental results. The study was performed on AISI 8620, a popular case-hardening, steel to understand microstructural and property effects for potential repair applications. The experimental samples were polished, etched with nital and picral for comparison, imaged, and Vicker's microhardness was taken at 0.5 and 0.2 kg loads. The etched images revealed a transformation zone slightly larger than the melt zone in all cases including a gradient in transformation along the outer edges of the transformation zones. The microhardness measurements revealed that the lower energy cases provided a higher hardness in the melted region even after tempering due to multiple passes. But the overall hardness was higher than what is to be expected of a fully martensitic structure in AISI 8620. The phase transformation model qualitatively shows a similar microstructure where molten regions turn completely to martensite. The model also predicts a transformation zone larger than the melt pool size, as well as the transformation of pearlite but not ferrite near but not in melt pool. This observation is experimentally verified showing a heat affected zone where pearlite is clearly transformed but not ferrite outside the transformation zone comprised of complete martensite. The hardness model predicts a lower hardness than the experiments but is similar to what is expected based on published Jominy End Quench tests. The cases in the regime dominated by conductive heat transfer show good agreement with the predictions of melt pool shape and hardness by the thermal model. However, at higher powers and lower speeds, the fluid flow influenced the shape of the melt pool and the heat transfer in its vicinity, and the model was less accurate.

1. INTRODUCTION

While additive manufacturing (AM) has received a great deal of focus in the scientific community recently, there have been relatively few attempts made to model mechanical properties based on processing inputs. There have been many groups that perform experiments to investigate mechanical properties and various processing effects in additively manufactured parts.[1]–[7] Other groups have created models to investigate the physics of the process or create a thermal model to investigate attempt modeling a “sound” part with minimal porosity.[8]–[14] But there seems to be few models that bridge that gap, taking processing parameters and attempting to create a model obtaining insight into mechanical properties. With the ability to accurately model these properties, experimental testing can be reduced and more directed with the guidance of a model. This reduction is useful especially in additive manufacturing as the cost of the powder for production can be prohibitively high.[15] The purpose of this work is to investigate current models for additive manufacturing and related processes to understand what has been done, and to put together a predictive model for hardness of a multi-phase steel(AISI 8620) and to validate it against a set of experiments. The model incorporates a phase fraction calculation which is the basis of predicting the local hardness, which is then compared to the experimental hardness values. To get a full understanding of how this model should be developed, investigation into past literature in laser welding, hardening, and cladding was done as these fields are very similar to the initial layers of AM. The model will only be looking at the first passes over a fully dense substrate and will not consider powder to help reduce variability. This allows initial experiments to simply be laser on solid plates. Other laser processes are considered due to varying circumstances that present similarities to the AM system. Laser welding is considered due to the continuous melting at a high temperature of similar materials which generates a large molten pool.[16] Since fluid flow can significantly impact the shape of the weld, reviewing this literature allows for understanding of fluid flow within the melt pool. Laser surface hardening is the process of creating a martensitic structure through rapid quenching as seen in steels. The literature focuses heavily on phase transformations in various steels so there is a great deal of literature discussing the transformations and calculation of hardness.[17], [18] This is useful as the current study is on a martensitic forming steel alloy. Laser cladding offers a look into the addition of a new layer on the existing material.[19] Which can give insight into understanding how each progressive layer will impact

those beneath. Of course, current AM literature will also be investigated for thermal modeling as well as understanding the aforementioned processes through current lenses.

Additive manufacturing is the process of building up a part from a finer constituent of the desired alloy. Parts can be fabricated out of strips, wire, or (most often) powder. Ideally, this process saves on material costs as all of the material is used and there is no need for an expensive mold or time to cut the parts to final dimensions. The parts made are typically close to the final shape and require minimal, if any, post-processing. Additively manufactured parts have been shown to have comparable or higher yield and ultimate tensile strengths than traditionally cast or machined parts.[15][20] Knowledge of stresses in use and freedom of design allows for reduced weight and makes this process highly favorable in industries where reducing weight is important such as aviation.

AM powder processes can be broken up based on the type of beam used to manufacture as well as the method of introducing the powder. The two types of beams used in AM are the laser and the electron beam. The electron beam is typically used for alloys that can be volatile if there is not a sufficiently low O₂ content as a vacuum environment is required. The powder is distributed by a coating arm onto a preheated build platform. The powder bed is pre-treated by the laser to begin sintering as it is important to be able to discharge the electrons used to melt the material as shown in Figure 1. The sintered powder can then be removed once the build is finished and if it meets the desired specifications can be reused.

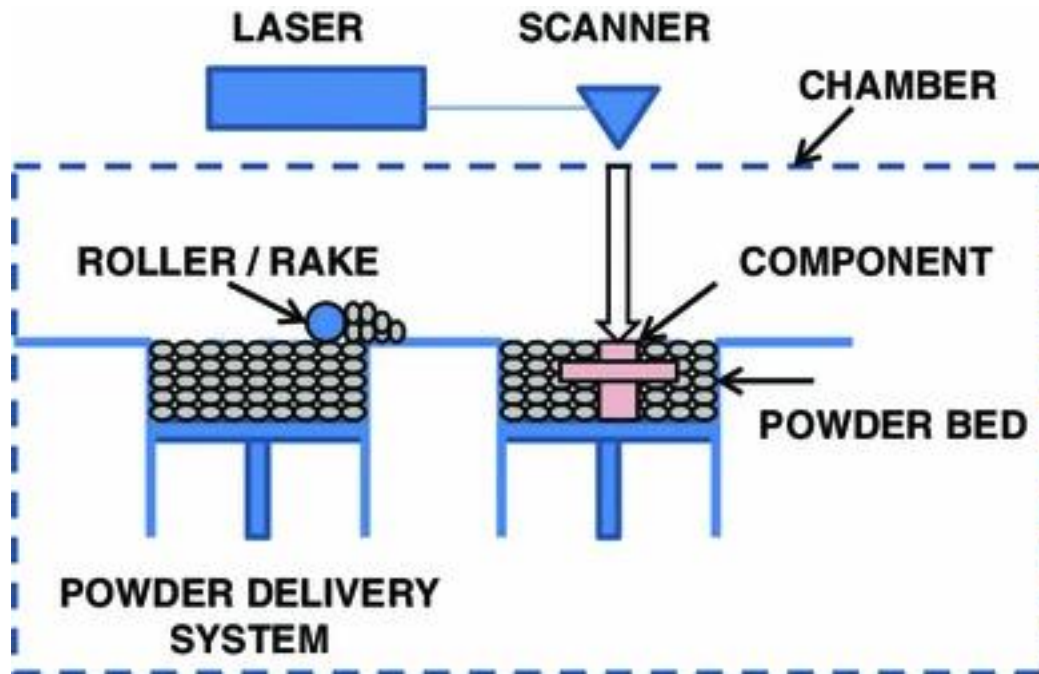


Figure 1: Graphic of powder bed fusion metal additive laser process.[15]

The laser-based processes can be sorted by the method of introducing the powder. There is laser powder bed fusion (LPBF) which is similar to the electron beam method, in that powder is drawn across a build plate for each layer. The major differences are the environment, typically an inert gas such as N_2 or Ar and the lack of significant build plate pre heat. The other major laser-based method is Direct Energy Deposition (DED) where the powder is carried in an inert gas and fired through nozzles into the path of the laser, there to melt and adhere to the melt pool below, as shown in Figure 2. This process can allow for free-building without supports, but typically has a rougher surface finish than the LPBF method.[15]

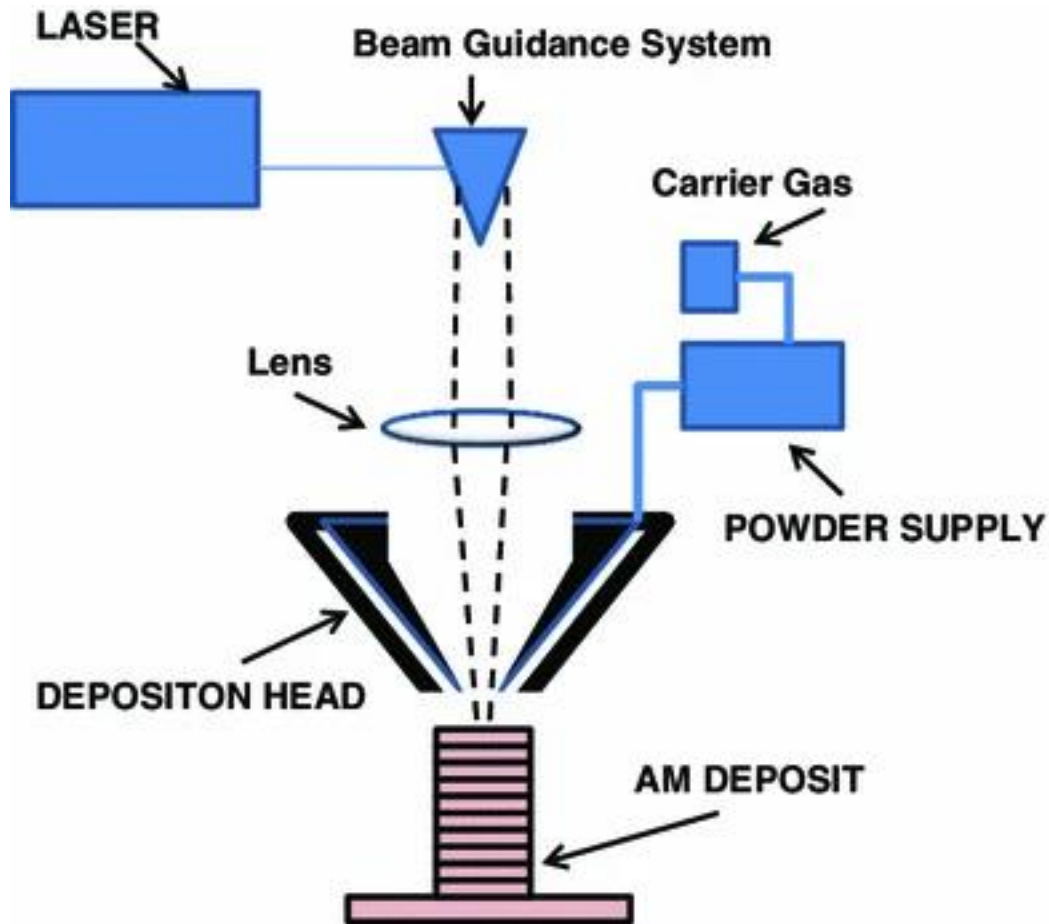


Figure 2: Graphic of DED blown powder laser additive manufacturing process.[15]

1.1. Background

Pursuing research in AM requires a visit to some past technologies that have been extensively studied and may hold the key to various issues in this relatively young field. Laser welding deals with the melting and intense thermal gradients seen in AM. Laser cladding investigates melting a new layer of a different material to a substrate. Finally, laser hardening focuses on investigation of phase transformations as the rapid quenching that occurs below the solidus temperature will form a new, stronger phase on the surface of the part being processed. While the quenching of the processed material occurs in all processes, laser hardening focuses much more on this process and subsequent tempering caused by progressive passes. This may not always be covered in welding as most welding consists of a single pass and laser cladding is more interested in interactions between differing materials.

An extremely important feature in laser welding is the characteristics of the heat affected zone (HAZ) that is directly outside the welded fusion zone(FZ). The HAZ is the area around the weld that reaches high enough temperatures that there are microstructural changes, causing a steep gradient in mechanical properties and makes the joint more prone to failure.[21][22] Understanding this region and how it can affect the final properties can lead to a better understanding of what can cause failure. The size of the HAZ can play a crucial role in the formation of cracks where a thinner HAZ is preferential to reduce likelihood of crack formation.[23] The size of the weld pool was shown to be tied to the peak temperature and the welding velocity. Increasing the peak temperature or decreasing the weld velocity would increase the HAZ size and its negative effects on the final part.[21][24] Because the purpose of the weld is to have a stronger connection point, investigating the hardness of the weld and the surrounding HAZ can lead to a better understanding of the size of the various regions. By being able to determine the hardness of the locations, the microstructure can be inferred and experimentally verified allowing insight into understanding how the various microstructure combinations will affect the properties. Being able to model these phases as well as the hardness can lead to a greater understanding of the overall process as well as a reduction in testing amounts. Hardness across a weld in M1500 steel was modeled by Wang et al, taking into account tempering and coarsening of phases.[25] They showed the strength reduction due to softening in the HAZ can be utilized to guide future weld optimizations. While AM is always done with multiple passes, understanding the size of the affected area around a weld line can give a general idea of whether tempering will occur and to what degree, in areas directly next to new laser passes.

Another important factor in laser welding is the melt pool shape, which is determined by the heat transfer fluid flow. A deep, narrow melt pool is ideal for welding so deep penetration along the joint can occur with minimal lateral melting. If the melt pool shape was determined solely by the heat conduction then the pool would always be hemispherical but that is not the case seen in welding. The melt pool shape has been shown to be highly dominated by the surface tension gradients of the liquid.[16][26] This Marangoni (surface tension driven) flow is caused by gradients in surface tension due to surface active elements and temperature.[27] The gradient with respect to temperature dominates the Marangoni number(Ma) which is a dimensionless parameter

comparing the rate of advective transport due to surface tension changes to the rate of diffusion of the liquid:

$$Ma = \frac{\left(\left|\frac{d\gamma}{dt}\right| * L * \Delta T\right)}{\mu \alpha}, \quad (1)$$

The surface tension gradient $\frac{d\gamma}{dt}$ is determined by the change in surface tension with changing temperature, L is a characteristic length, ΔT is the change in temperature, μ is the dynamic viscosity, and α is the thermal diffusivity. The surface tension gradient will determine the sign of the Marangoni flow depending on how the surface tension changes with temperature. If the surface tension increases with temperature then the gradient will be positive and if the surface tension decreases with increasing temperature then the gradient will be negative

When convective flow dominates the Marangoni number, if the surface tension gradient is positive, then as the melt heats up, the hotter liquid is driven down to allow cooler liquid to take its place to reduce the overall surface tension of the liquid. The hotter liquid is driven deeper into the center of the weld pool, transferring a large portion of heat to the bottom of the pool before rising again. A negative surface tension gradient will have the opposite effect, causing a wider melt pool as the hotter liquid is driven across the surface to the outer edges before descending as have a larger interface between the liquid and air is preferred that solid to air interface. The effects of surface tension gradient on the direction of Marangoni flow are illustrated in Figure 3.

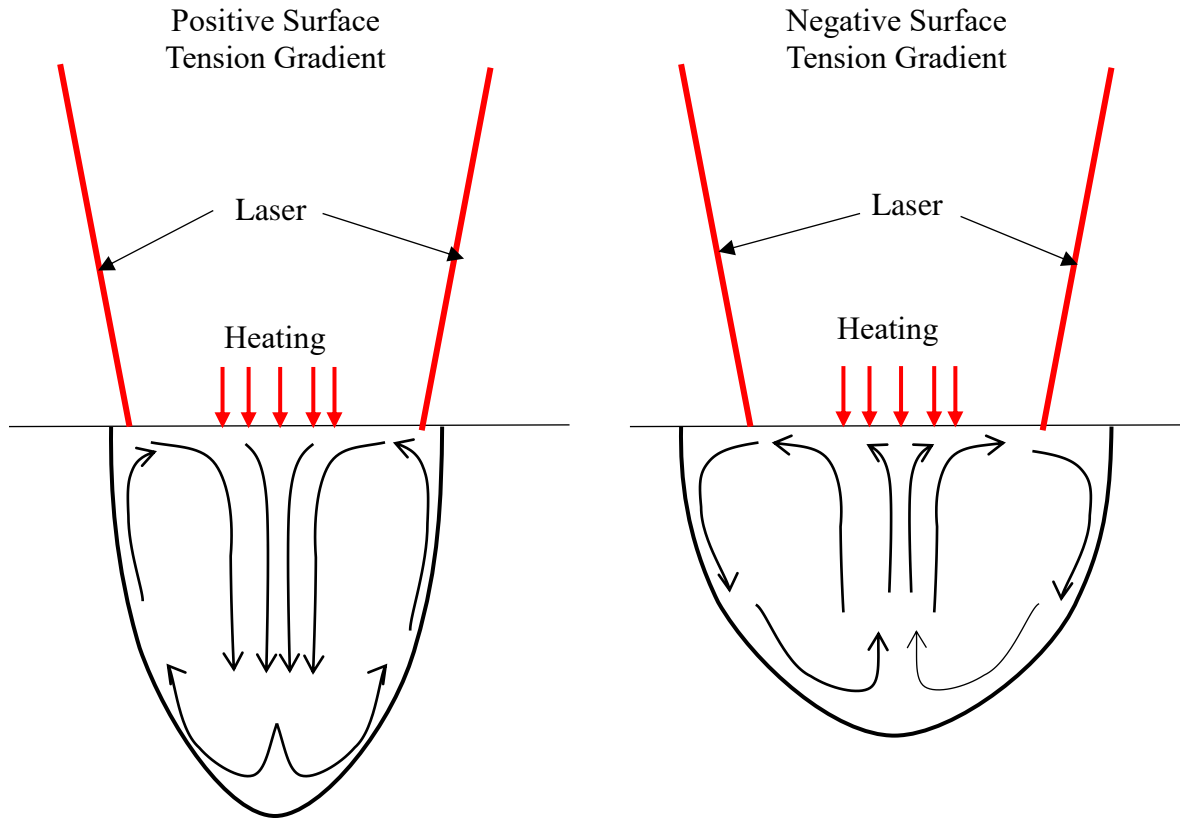


Figure 3: Visualization of surface tension gradient on the melt pool fluid flow.

A negative surface tension gradient will help achieve more contact between passes on the same layer but will weaken inter-layer connectivity. Having too positive of a surface tension gradient will mean lower power and speeds will be required to not cause porosity formation. A narrow weld pool can cause pores between weld lines as well so understanding the effects of surface tension gradients are important for each material in AM to be able to fully understand the strength of their effects.

Laser cladding has an extremely similar setup to the DED method shown in Figure 2, with blown powder flowing into the path of a laser and melting to the substrate. The main differences are the goals of the two processes. Cladding deposits a layer of a different, usually harder or more wear resistant material than the underlying substrate.[19], [28], [29] To this end, controlling the microstructure and properties of the deposited layer is important in producing the desired properties in the new layer. The zone between the two layers where the powder first contacts the molten substrate can have different properties than either of the two layers because of partial melting of the substrate and mixing with the deposited liquid.[28] Mixing of the layers cannot be avoided to ensure there is a proper bond between the layers but minimizing the dilution factor

within these limits can greatly increase the strength of the cladding as deleterious phases are less likely to form with low dilution.[29][30] To help decrease dilution, an ideal power density should be found to keep the melt pool from being too deep causing high dilution or inadequate bonding between the layers. Finding the correct energy density range also helps to idealize the shape of the cladding as well to help adhesion and ensure that no other defects such as pores or cracks form in the clad layer.[31] A cladding that is completed in multiple passes will be softer than a single line pass due to the heating causing tempering of the previous pass.[30] In a steel based cladding, it is important to know how much tempering will occur to ensure that the clad layer will be able to perform the desired task. While, there is typically only interaction between two materials in the first layers of AM that are typically removed, it is still important to be able to understand the microstructure evolution especially in multiple passes causing rapid heating and cooling. While there may be multiple layers in a clad sample, the most important area of research tends to be the first layers and adherence with the substrate as this is the most likely section to fail either by poor adherence or brittle phases causing the clad layer to break off.

The final process for discussion prior to investigating AM is laser hardening which is commonly used in steels and Titanium alloy systems. This process focuses on maintaining a completely solid hot zone which is then quenched through conduction into the bulk so that a martensitic phase change can occur, thus hardening the surface without adding material or negatively impacting the underlying bulk. As the name implies, the focus of this process is hardening to increase wear and fatigue resistance.[32] In steels, this process calls for heating only into the austenitic region, followed by a rapid quench to form martensite. This process is simple for a single pass as long as melting does not occur but becomes difficult for multiple passes. Due to the radial distribution of heat from the laser location the hardened zones appear as hemispheres in 2-D as shown in Figure 4. The hardened zone(HZ) is the zone that is austenitized and quenched to martensite, while directly outside that region is the HAZ similar to welding that was affected by the heat but was not hot enough to transform.[32] This process becomes more complicated as more passes are added, as the new pass will temper part of the previous pass. Ideally, the surface hardened properties are uniform across the entire zone, so any tempering of the previous passes is an undesired effect. Balancing overlap so that the depth of the hardened zone is uniform with the amount of tempering of the previous pass is of high importance. This backtempering process relies on the initial

microstructure formed by the first pass and the thermal history caused by the second. The second pass will overlap with the first, reaustenitizing some of the first pass, but there will also be a HAZ in the original HZ which will be slightly softer now due to this effect, as seen in Figure 5. Lakhar et al predicted the phase transformations and corresponding hardness in a two pass process with AISI 4140 steel with quenching and tempering and was able to show control of variation in hardness by amount of overlap.[17] They showed good agreement between the model and experimental results.[17] Fortunato et al built upon this work by evaluating the time at temperature during the laser hardening process. They found that the time spent at an elevated temperatures were so short that carbon diffusion rates were greatly impacted in the HAZ and tempered regions.[33] In the HAZ, pearlite colonies have a fine structure so little time is needed to homogenize the colony and then transform it to austenite. Adjacent ferrite was so carbon depleted, and there was not enough time for more carbon to diffuse into it, that it did not change to austenite. A similar effect is seen in the tempered region which would cause a larger gradient of hardness within that region where the time at elevated temperatures would cause a larger gradient in the amount of tempering.[18], [33], [34] They show that taking an integral transformation time to evaluate differences in the phase transformations not occurring exactly at the equilibrium rate matches closer in the tempered region than previous works. The works showing that laser hardening has some speed dependence based on backtempering and initial cooling rates and it can be assumed that AM processing will have a similar dependence as the laser is much smaller and traversing at a much higher rate causing much higher temperature gradients to be occurring.

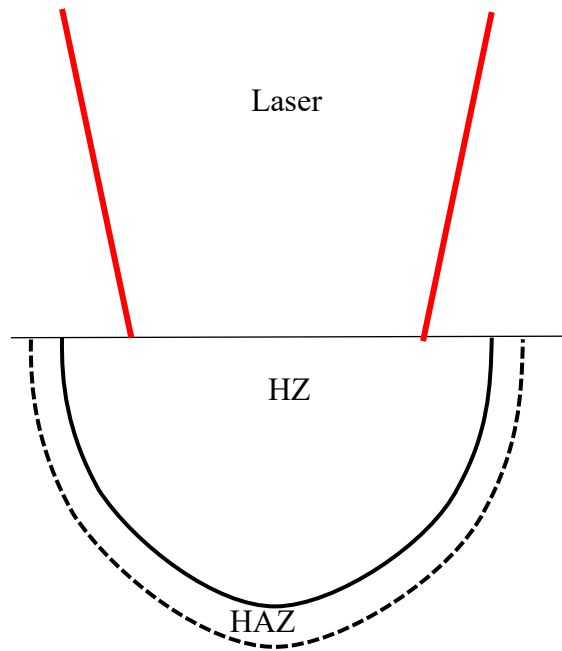


Figure 4: Schematic of laser hardening, showing the hardened zone (HZ) and the adjacent heat affected zone (HAZ).

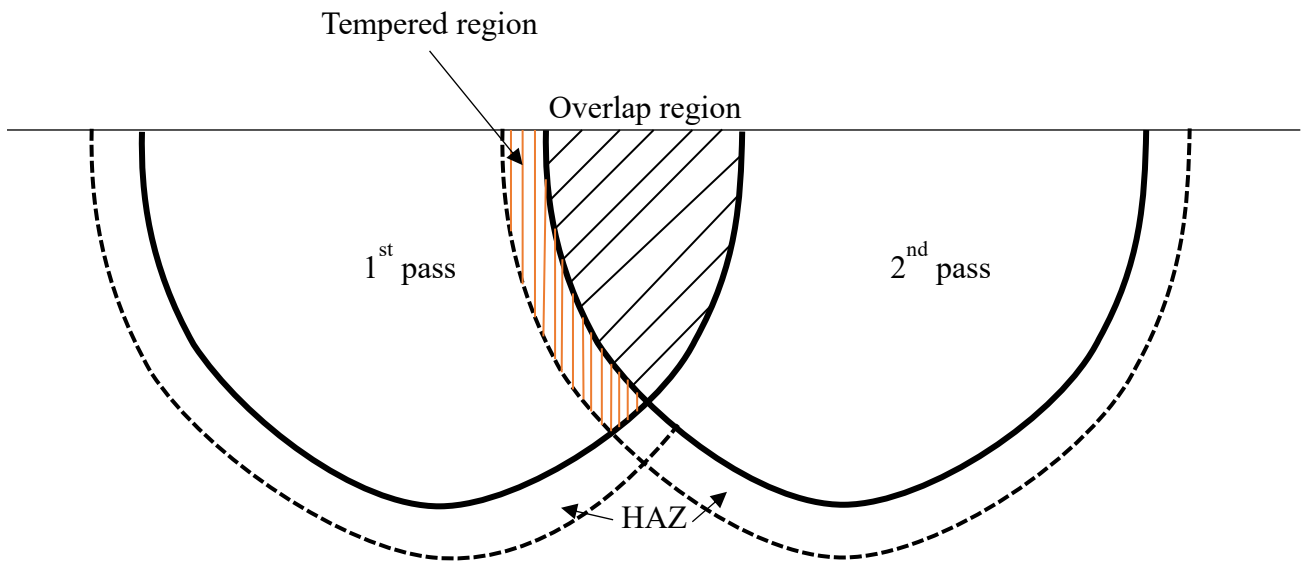


Figure 5: Schematic of two pass laser hardening showing the overlap of the second pass onto the first where retransformation occurs and tempered region.

1.2. Initial Investigations into AM

As the field has grown in feasibility and uses, there has been a large drive to understand the mechanical properties of finished parts. Understanding the thermal cycling has been paramount to this effort as the laser typically ranges from 10s to a couple 100s of μm . Due to the small size of the laser there is little change in local composition so the composition is greatly determined by the feedstock used so, assuming no porosity the dominant feature that affects mechanical properties is grain size and morphology. While achieving low porosity has been an issue there have been significant strides in understanding processing and material parameters to help reduce porosity across multiple materials. Porosity can be formed a number of ways and have been conveniently classified in Ti-6Al-4V by Gong et al. across three major regimes: fully dense(region I), over melting(region II), and incomplete melting(region III).[35] The fully dense region is considered free of porosity while porosity in the incomplete melting is due to particles and layers not fully sintering together. This can be caused by a number of issues such as low power input to sufficiently melt the particles from either too large of a laser velocity or insufficient power from the laser. Another potential cause of this is a large hatch spacing between laser passes causing the passes in plane or layer on top of each other to not fully bond or fill. The over melting regime is caused due to laser power is either too high or velocity too slow it is causing vaporization of the material creating gas pores entrapped in the solid. The overheat regime (OH) is an extreme regime where builds fail due to thermally induced stresses causing jamming of the recoating process. Their experimental space and classification of zones can be observed in Figure 6.

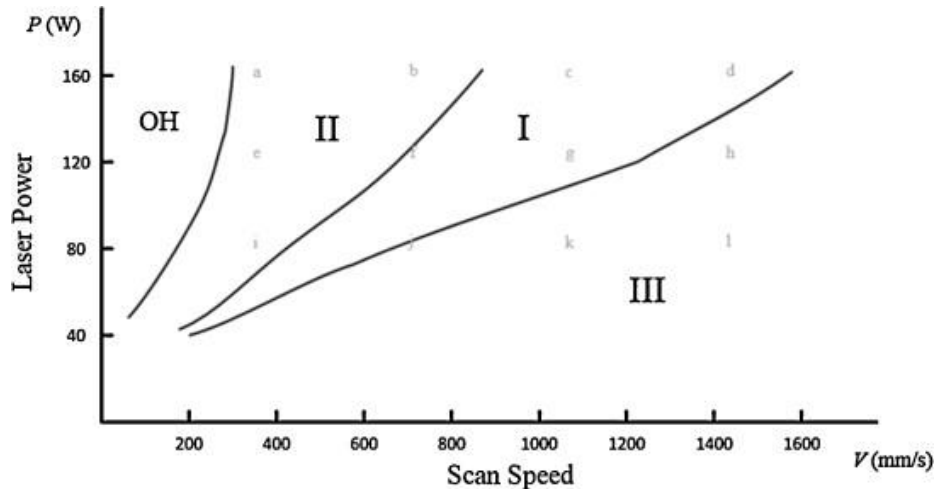


Figure 6: Process window for SM Raynor Ti-6Al-4V powder. Section I is the fully dense, II the over melting, III the incomplete melting, and OH is overheat regimes[35]

Bean et al did a similar investigation into porosity in Inconel 718 but focused on laser focal shift showing a dependence of porosity on laser size and energy density within the melt pool.[36] They show that for a given set of laser parameters there is an optimal laser focus which can effectively determine the melt pool size and energy density which can determine whether full melting, partial melting, or over melting will occur. While the current focus is not on porosity it is important to understand that there have been many studies identifying parameters that impact the melt pool to achieve the highest density possible parts so that accurate calculations and experiments can be performed to understand mechanical properties of parts made in this new process. Once the builds can be assumed fully dense understanding the underlying morphology of the structure can be assessed.

Porosity and energy density have not been the only studies into AM thus far. Special consideration has been given to the plume and ejecta from the melt pool. The plume is the vaporized material caused by the intense heating at the center of the melt pool and as the vapor comes off it reacts with the ambient atmosphere and can interfere with the laser. While larger ejecta are full powder particles that may have partially or fully melted but were ejected from the melt pool for a variety of reasons. These larger particles do not directly interfere with the laser but may cause defects in other ways. Nassar et al created an effective visualization of this shown in Figure 7. Nassar et al looked at the varying types of large ejecta that came out of the melt pool and their effects on defects. Large ejecta formed from partially or fully melted powder particles that coalesced in the air and was deposited elsewhere. These ejecta can lead to porosity in areas that they vacated or where they land as they may be too large to melt fully when the laser passes over them.[13] This process was also modeled by Khairallah et al using finite element modeling(FEM) to track the liquid surfaces to determine how fluid flow could eject large particles.[14]

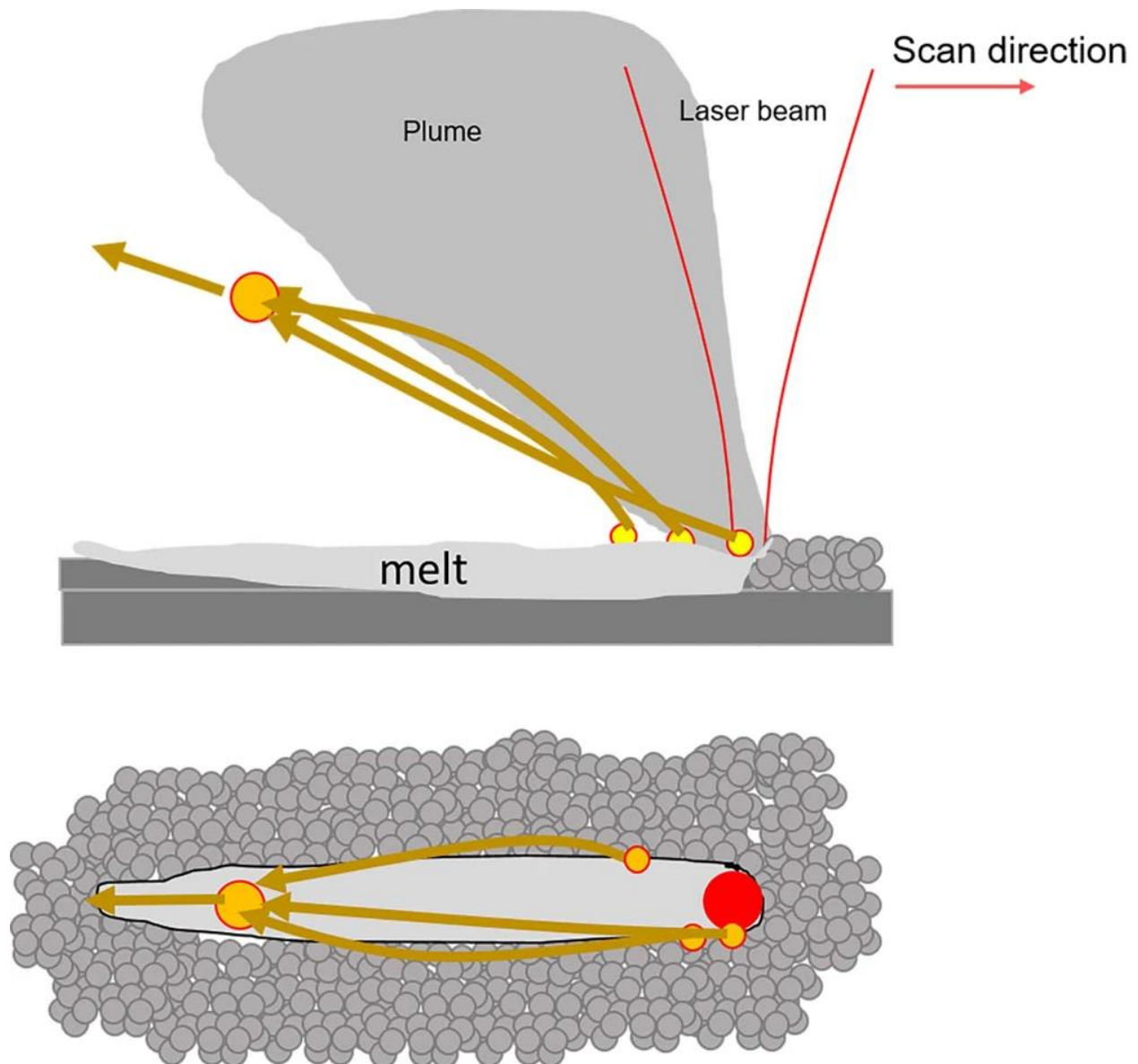


Figure 7: Illustration of laser passing through a powder bed showing the plume(gray) of microscopic sized particles and macroscopic ejecta(yellow).[13]

The ejection of the particles was also investigated by Liu et al where they did single passes to understand the denudation of the powder based on the energy density. They showed that an increase in energy density created a larger denuded zone and the particles ejected in the higher energy density cases had many satellites attached which hurt the properties of builds that utilized the same powder afterwards.[7]

Analysis of the plume has also been of interest as the smaller particles are known to scatter and reflect the laser energy. This is a well-known phenomenon in laser welding and is known as something that cannot be removed. The positive in welding is that there can usually be a much stronger airflow to control the plume size and reduce its effects.[16] But in AM, in a closed box with very fine powder it is unwise to use a high airflow to remove the plume. The welding plume has been modeled by Pang et al in an attempt to understand its dynamic motion and how this information can be used to predict weld pool size.[37] Other works have looked into methods on how to control the size of the weld pool by changing the shielding gases used as well as the ambient pressures. Bidare et al investigated lower and higher than normal atmospheric pressures to see the effect it had on the plume. The higher pressure did a better job at suppressing the plume but caused the melt pool to stay hotter longer.[38] While it was not the focus of the study, this increased temperature and slower cooling time could drastically alter the microstructure. On the other hand, the lower pressure caused the plume to grow much larger and in turn due to the reduced atmospheric pressure increased denudation which reduced the weld bead size as there is less material in the location for melting.[39] Bidare also investigated differing shielding gasses that what is currently used. Current standard is either pure N₂ or Ar flowing gas. But Bidare investigated utilizing He gas as a shielding gas and found that due to the higher thermal conductivity that it allowed even faster cooling for potentially more control over the microstructure.[38]

Powder morphology can play an important role in the quality of the final part by impacting flowability, packed bed density, and final build properties.[6], [40], [41] Liu et al looked at the effect of two powder size distributions of AISI 316 stainless steel. Both lots had the same final mesh size but the distribution between the particles was different. They found that a larger distribution created a more packed structure at lower powers while a more uniform distribution created harder and stronger parts.[40] Tang et al investigated the effect of reuse of the powder between builds in Ti-6Al-V4 powders. They observed an increase in oxygen content in the powder which in turn increased the strength. But they also noted a narrower particle distribution due to sintering of smaller particles to larger particles. Due to the roughening of the powder, surface roughness increased in the parts built in later reuse cycles.[41] Averyanova et al investigated the actual powder properties of 17-4PH steel to see how changes in initial microstructure can impact

final microstructure. The change in microstructure is typically governed by slight changes in composition. In the case of 17-4PH, they had two powders, one that was mostly martensitic in structure and one that was majority retained austenite. They processed these powders and noted a distinct difference in final microstructure as well as hardness.[6]

There has been some modeling of the AM process as well. King et al at Lawrence Livermore national lab describe a thermal model being able to predict builds in powder as well as a FEM model to track fluid flow in the weld pool along with powder flow.[42][43] Criales et al created a predictive model that, given the material inputs, could perform a multi-variable optimization based on final part density, processing speed, and energy density and were able to show good agreement with experimental results for IN625.[11] Mukherjee et al created a thermal model that could be used across a variety of materials and predicted dendrite formation as well as proper spacing to avoid inter-weld defects.[44] Wang and Felicelli modeled a multi-layer build that was one weld line thick and observed the martensite formation and tempering in the build in a build of AISI 410 stainless steel. They found that controlling laser power was needed to ensure a continuous, predictable microstructure but there would always be some tempering of earlier melt pools. This finding was supported by their experimental results showing lower hardness in the first layers deposited, with the hardness increasing to a uniform, higher value in later layers. [12] Costa et al had similar findings of hardness distributions and phases while modeling AISI 420 tool steel. But they too also only reported a thickness of one element in their FEM.[45] While these studies are in agreement, few AM builds are only one layer in width. Adding more passes in a layer could potentially alter thermal gradients and thermal distributions throughout the build as it is now not in a single pass width.

While these models cover a comprehensive array of thermal modeling and microstructural evolution, they are either thermal models, using temperature and phase change simulations to predict the feasibility to produce fully dense parts, or microstructural models, capable of simulating only a very small volume. Coleman et al modeled laser melting on a substrate while tracking the temperature, gradients, and solidification of multiple passes.[10] They determined that within certain processing parameter ranges, the impact of Marangoni flow and subsequent fluid motion does not need to be considered to accurately depict the melt pool shape and heat transfer.

Neglecting fluid flow drastically reduces computation time allowing for larger cases to be run. While the thermal effects can be seen through a spike in temperature at the surface due to vaporization, there is no physical change to the test mesh. This thermal model can be expanded upon by coupling microstructure prediction based on the calculated transient temperature histories, given that the required thermophysical properties and phase transformations of the alloy are known.

While laser-based AM methods can have various methods of powder delivery and design set-ups, the one constant between all the processes is that the material will get rapidly heated, melted, and then immediately quenched within fractions of a second. Parts have multiple laser passes happening either right next to each other or right on top of each other, so a given section can undergo heating and cooling cycles many times in the course of a build. It is important to understand how the microstructure will evolve to ensure desired material properties. Of course, every material will have different types of phases present and so will respond differently to the thermal cycling, but there are two variables that are part of every microstructural system that impact mechanical properties: the grain morphology and the phase fractions present within those grains.

1.3. Mechanical and microstructural property analysis

AISI 8620 is a case hardening steel that is commonly used for applications requiring high wear resistance. Alloys similar to 8620 are used in the aviation industry for gears and other low-temperature rotating parts.[46]–[48] Eventually these parts wear or crack and must be replaced, but repair may be a possible alternative using AM. To determine repair feasibility, understanding this alloy's responses to the AM process would be highly beneficial. Unfortunately, because alloy steels are not typically welded to avoid detrimental martensite formation, there is little information on welding or AM processes of these kinds of alloys. A basic understanding of the changes in properties and microstructure would provide a good start in determining the use of this process for these alloys.

Hardness is one of the easiest ways to begin to characterize the processing effects on properties. The hardenability of steels can be determined by the Jominy end quench test as the kinetics of the

phases changes in steel is well known. AISI 8620 has established end quench curves accumulated in Reference [49] and is shown in Figure 8. The expected maximum hardness for this alloy when at 100% martensite is ~470 Vickers Hardness based on this information. With the rapid quenching in AM, hardness values can be expected to appear around that value.[49]

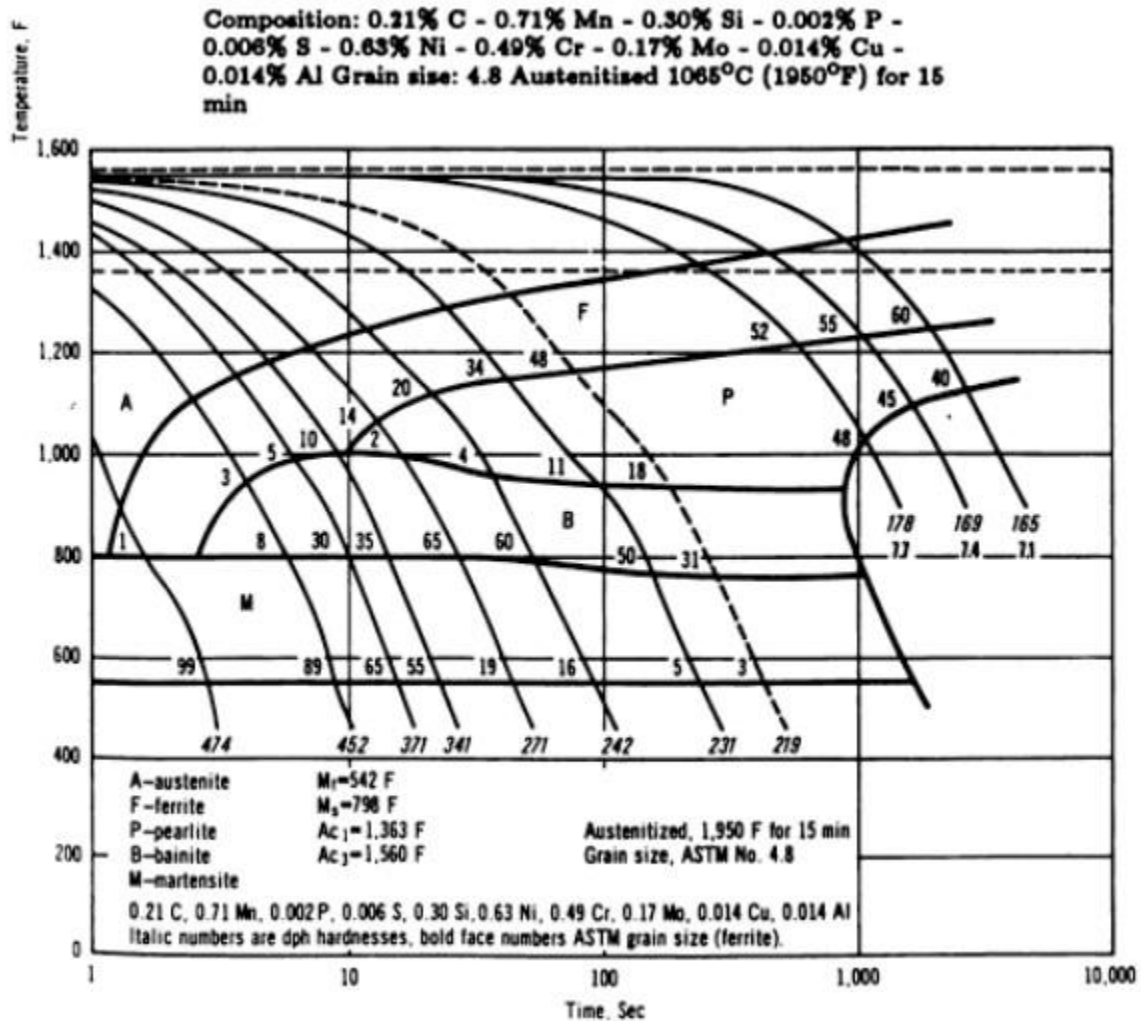


Figure 8: Jominy end quench hardiness results across a time-temperature-transformation diagram for AISI 8620.[49]

Etching the samples after processing can give insight into the distribution of phases and with the correct etchants can reveal other finer details of the microstructure. Nital(5% nitric acid, 95% ethanol) and Picral(2-4g picric acid in 100ml ethanol) are two such etchants that are commonly used on steels. Both etchants attack the ferrite structure in steels, but the metal's response to nital

is dependent on the crystallographic orientation as well as revealing ferritic grain boundaries which can impact visualizing of some finer features. Nital is also a slower acting etchant so there can be more control over the degree of etching that occurs.[50] Looking into etchants across a wide array of materials, while etchants are typically reported, the desired attributes of the microstructure accentuated by the etchants is not. Moussaoui et al used aqua regia for etching Inconel 718, while Zhao et al used an electrolytic etch of H₂O, HCl, and H₂O₂ to do microstructure analysis.[51], [52] Yet still, Trosch et al use a mixture of lactic acid, oxalic acid, and HCl for an electrolytic etchant.[53] Zhang et al used Kallings etchant(cupric chloride, HCl, and ethanol) for their investigations into Inconel 718.[54][20] Steel etchants, even within a small group in AM, range just as widely as shown in Table 1. While these are the ones who reported etchants, there are also many groups who did not report an etchant at all. In fact, only Wang et al mentioned what their etchant would attack and what they hoped to view from it. But they ended up having to use a scanning electron microscope to view the grain structure as their chosen etchant did not provide them with that information.[4] Understanding the effects of the chosen etchants and what information can be gleaned from their use can make investigation of microstructure simpler and more informative.

Table 1: AM steels and etchants used.

Steel	Etchant	Reference
17-4 stainless	10% oxalic Modified Fry's reagent	[55]
17-4 PH stainless	Electro-etch with 40% nitric acid	[56]
AISI 316L	Tripartite solution: HCl, Nitric acid, H ₂ O	[57]
H 13 tool steel	2% Nital	[58]
17-4PH stainless	CuSO ₄ , HCl, H ₂ O	[59]
AISI 304L	NaOH, H ₂ O	[4]
17-4 PH stainless	Electro-etch with HCl, ethanol, and CuCl ₂	[60]

1.4. Overview

With current AM literature showing few models connecting the processing conditions to mechanical and microstructural properties. Utilizing the literature in similar fields, a model can

be created to predict microstructural changes based on the thermal processing. This can be compared to experiments to determine accuracy and applicability. AISI 8620 steel was chosen due to the martensitic transformation and subsequent tempering caused by large thermal variations in steel. This allows for visual tracking of the thermal processing based on these transformations and can be evaluated for impact of individual weld pools and interactions between weld pools. Thus, the aim is to be able to expand the thermal model to include microstructure prediction to predict hardness and microstructure across a multiple pass per layer build volume and being able to understand the thermal history leading to these predictions.

2. EXPERIMENTAL STUDY OF LASER MELTING

AISI 8620 steel is a popular welding alloy and is a similar composition to alloys used in the aviation industry for case hardened, non-rotating parts such as gears.[48] As these gears were, they are eventually taken out of service and discarded. While repair would be an ideal option to increase the lifetime of these parts, current repair methods such as DED do not provide enough dimensional accuracy for these parts. Potentially utilizing the powder bed fusion technique could yield increased dimensional accuracy and allow for repaired parts to be put back into service. But the microstructure and effects on properties based on this process are not well known. Initial experiments on AISI 8620 steel can yield insights into the microstructural effects of the powder bed fusion process and can provide insight into the applicability of this method for repair of these parts.

Physical laser melting experiments were performed on AISI 8620 steel disks at OakRidge National Lab. Six test cases were chosen based on literature review, ensuring hatch interaction, single- and multi-track over a range of power and speed. The samples were cut so the cross-sections were exposed in the center of the weld to ensure the steady state condition was being evaluated. The weld cross-sections were etched with nital and picral etchants to investigate variations in etchant quality and visible features. Micro- and nano-indentation were performed to understand how varying process conditions affected the distribution of hardness and microstructure in single pass and multi-pass welds. The shapes of the melt pools were used to guide the surface tension gradient calibration for the thermal model.

2.1. Choice of process parameters

Before choosing experimental process parameters, a literature search for steels in AM was done to find suitable values. Some of the parameters from various sources are presented in

Table 2.

Table 2: Parameters for Powder Bed Fusion AM for steels found in literature

Material	Speed(mm/s)	Power(W)	Line Spacing(μm)	Layer Thickness(μm)	Reference
17-4	1000	195	100	20	[55]
17-4	800	195	100	40	[55]
AISI 316L	600	150	80	40	[7]
AISI 316L	300-800	104	130	30	[61]
AISI 316L	250-500	104	130	30	[61]
AISI 316L	400	100		30	[1]
17-4PH	1000		100	20	[60]
AISI 316L	50	120	120	40	[62]
AISI 316L	50	100-300	80	50	[40]
AISI 316L	87	150	130	75	[5]
AISI 316L	175	80-200	40-60	100	[63]
AISI 316L	1500	200	84		[64]
AISI 316L	1200	200	104		[64]
AISI 316L	800	200	123		[64]
AISI 316L	500	200	121		[64]
AISI 316L	1200	150	79		[64]
AISI 316L	800	150	109		[64]
AISI 316L	500	150	115		[64]

There is a clearly wide range of parameters used even for the same alloy of steel so it is clear that there are a wide variety of potential parameters that can be used given the information presented. Without finding any data on the AISI 8620 steel being used, a matrix on the higher energy density side of these parameters was used to ensure that the laser lines were fully formed and would overlap in the hatched region to be able to investigate multi-pass interactions. A “sanity check” case was performed at a higher laser beam velocity in a region that was expected to not have any overlap in the hatching region.

Something that was not always reported was the laser radius, defined as the full width half maximum of the laser, which can have a strong impact on the energy density. It will greatly impact the size of the melt pool and how the energy is directed into the part. While energy density is not an accurate way of predicting the size and shape of the laser lines it can give an idea of how much energy is traveling through the piece. Energy density, $\left(\frac{J}{mm^2}\right)$, is calculated from laser input parameters shown in Equation 2:

$$E = \frac{P}{hv}, \quad (2)$$

where P is the power of the laser in watt (W), h is the hatch distance between passes(mm), and v is the laser scanning velocity (mm/s). Typically, a layer height term is included in the denominator, but since there will be no additional layers added the term is omitted.

2.1. Sample Preparation

A bar of 2-in diameter normalized AISI 8620 steel was procured from McMaster-Carr and cut into 1-inch thick pucks. Three pucks were cut with a bandsaw and ground flat and parallel with a surface grinder. and leveled using a surface grinder to ensure that there was no angling caused by the placement in the abrasive saw. The pucks were then polished to a 2000-grit surface finish to grind away any potential surface hardening caused by the surface grinder following the listed grits in order: 180, 320, 600, 800, 1200, and 2000. The pucks were then sand grit blasted to increase the randomized roughness of the surface to help increase absorptivity and reduce direct reflection back into the optics of the laser. The finished pucks can be seen in **Error! Reference source not**

found. and chemical composition of AISI 8620 can be found in **Error! Reference source not found.**

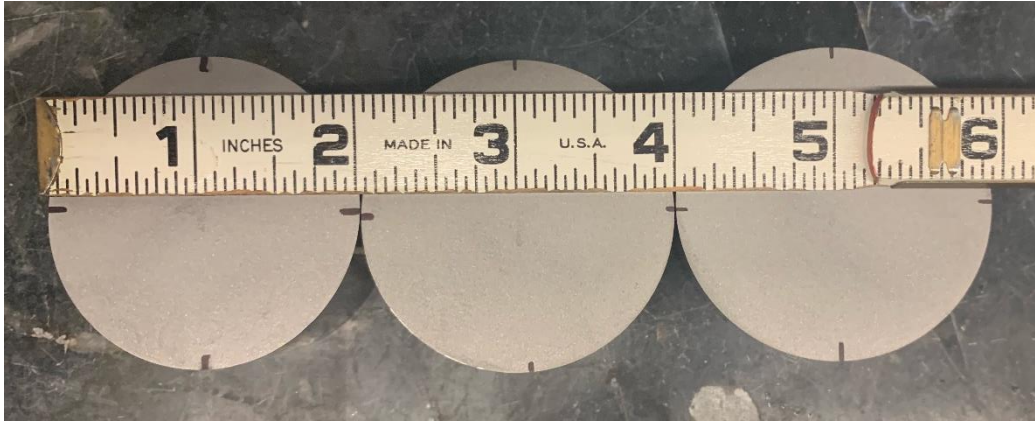


Figure 9: Finished sample pucks ground to the same height and grit blasted taken using cellphone camera.

Table 3: Composition of AISI 8620.[65]

Element	C	Cr	Mn	Mo	Ni	P	S	Si	Fe
Composition	0.18-	0.4-	0.7-	0.15-	0.4-	<0.04	<0.04	0.15-	Bal.
wt%	0.23	0.6	0.9	0.25	0.7			0.35	

2.2. Choice of Build Parameters

The pucks were laser at OakRidge National Lab using a Renshaw AM250 additive machine. The build platform was lowered so that the surface of the pucks was in the plane of focus and processed in an inert Nitrogen atmosphere. The Renishaw AM250 utilizes a Nd:Yag pulsed laser. The pulse rate was set high enough compared to the velocity that its effect on the temperature field was effectively the same as a continuous laser. These pucks were processed using the parameters shown in Table 4.

Table 4: Processing parameters for the six chosen speeds and powers to be put on the three pucks

Sample	Speed (mm/sec)	Power (W)
1	700	195
2	400	195
3	300	150
4	200	125
5	200	195
6	400	125

Each puck held two processing conditions with three individual laser passes and one multi-pass rastered region as in Figure 10a and a completed example can be seen in Figure 10b.

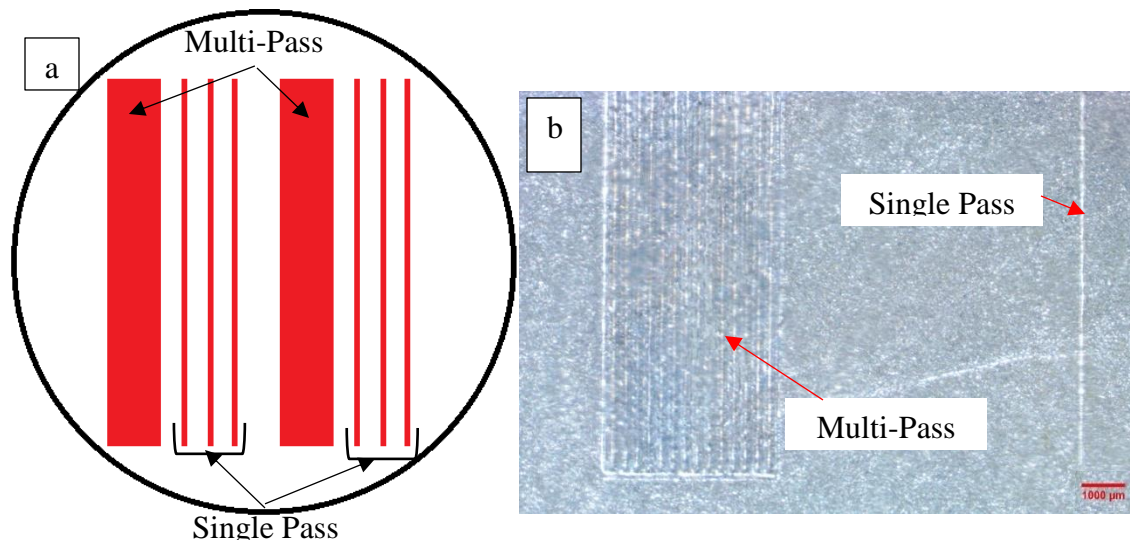


Figure 10: Visual of the layout of the hatch region and laser passes on the top surface of the puck(a). Stereoscope top-down image of completed hatch and one single line test case as processed(b).

All individual tests were spaced far enough away from each other so there would be no meaningful thermal interaction among the test areas. In all cases, the length of the weld was 2.54 cm, the hatch spacing was 100 μm , and the laser radius was assumed a Gaussian distribution with a full width half medium of 70 μm .

The lased pucks were then sectioned so that a central cross-section of each set of parameters could be observed. The cut surfaces perpendicular to the laser direction were polished and etched using both a nital and picral etchant to evaluate which etchant allowed for better visualization of the desired phases. In the nital etch (5ml nitric acid and 95ml ethanol) samples were immersed for 10 seconds and later in the picral etch (100ml ethanol and 3g of picric acid) for 1 minute. The samples were imaged using a light optical microscope as well as a Phenom 650 FEG scanning electron microscope using the secondary electron sensor at 5 kV. Micro- and nano- indentation were performed across various sections of the multipass area as well as the single pass areas to evaluate tempering effects and parameter effects on changes in hardness to be evaluated against visible changes in phases. The hardness measurements are used to find mechanical properties distribution in relation to the microstructural distribution and to compare to the predicted model hardness. Vickers microhardness was performed with a 0.5 and 0.2 kg loads using a diamond pyramid tip, producing an indent approximately half the width of the melt pool to obtain an area of effect solely within the melt pool. For the multipass cases, two different locations were investigated: the melt pool areas unchanged after melting and resolidification, and areas altered by subsequent passes, and the area that appears to be affected by subsequent passes. This phenomenon is explained in Section 2.3.3.

2.3. Results

2.3.1. Preliminary metallography with Nital and Picral etchants

Before characterization of the samples took place, an investigation of various etchants was performed to get a better understanding of the microstructure and see if there were any major features missed or covered up by specific etchants. The most common etchants used for ferrous steels are nital and picral. While nital is far more commonly used due to relative safety factors, it can hide some features. Picric acid is combustible if allowed to dry out so is less commonly seen

to reduce hazards in the lab if no clear advantage is seen. A comparison of the etchants of some multiple pass experiments can be seen in Figure 11. The ferrite grains and pearlite colonies appear to be evenly distributed in the bulk, with large ferrite structures distributed throughout the matrix. This microstructure is expected as AISI 8620 is a pro-eutectic steel in which ferrite would be the dominant phase.

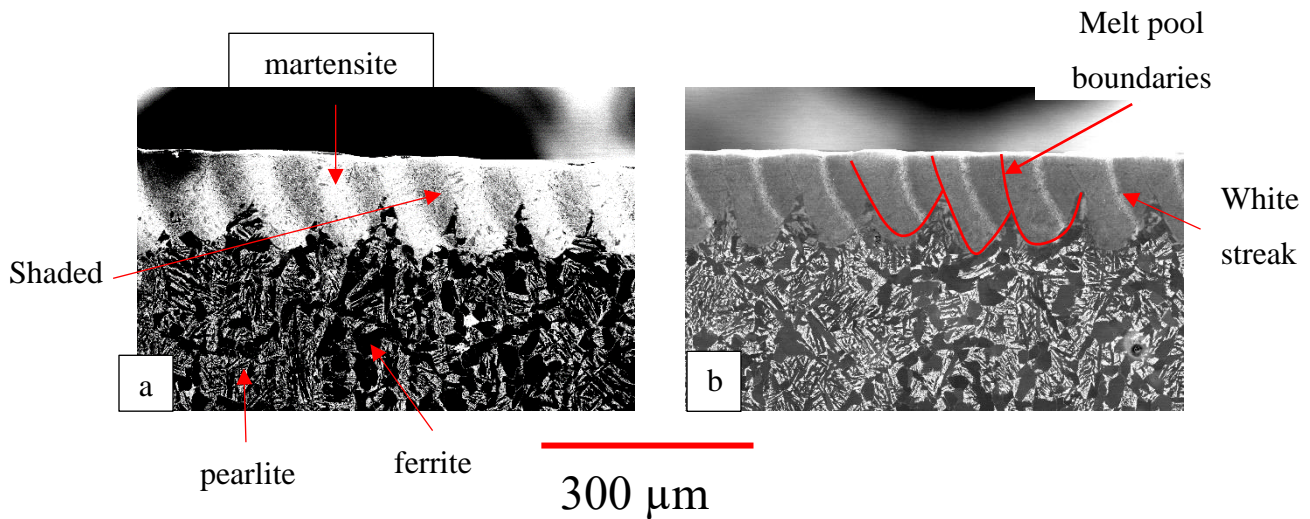


Figure 11: SEM images of multi-pass experiments etched with nital (a) and picral (b) processed at 200 mm/sec and 125 W.

In Figure 11(a) with the nital etch, the melt pools can be clearly separated from the unaffected bulk material. The pearlite and ferrite grains in the bulk can also be identified. There appears to be a shaded region (different contrast) on parts of each pass which appear to have additional processing after the initial pass that melted it. It is possible to identify the martensitic structure of the weld pools but it is hard to accurately identify any smaller features. The picral etch in Figure 11(b), on the other hand, shows a much less busy image. While the martensitic grains in the melted regions cannot be individually identified, the differing phases can be, which is enough for the general microstructure. Looking closely at the hatches, the edges of the melt pools can be clearly seen indicating the laser passes progressing to the right. While not easily seen in the nital etch, it can be inferred after close evaluation, but the melt lines themselves cannot be seen where there is overlap but can be seen in regions where they are not remelted in later passes. The edge of the melt pools can be more easily seen in the single pass cases shown in Figure 12(Section 2.3.2). The

shaded regions in the nital etch now very obviously correspond to the tempered regions of the previous passes. This is bounded by a white streak in the picral etchant where the temperature of the piece to the left of that line would have minimal tempering while to the right all the way to the weld line there would be a great deal of tempering expected. All micrographs shown in later will be etched with picral unless noted otherwise since picral allows more detail to be seen in and around the melt pools.

2.3.2. Single Line Experiments

Figure 12 shows the single pass weld lines and the microstructures for power-velocity test matrix conditions (Table 4) with the highest energy density case being scaled differently due to scaling issues caused by the weld pool depth being much deeper than the other pools. The melt pools became deeper with increasing power at given velocity and with decreasing velocity at a given power. At the slowest velocity and highest power, the melt zone shows a keyholing shape deviating greatly from a hemispherical shape and showing gas pores created from gas entrapment under the melt pool. The highest velocity, lowest power zone maintains the hemispherical shape of a weld pool not dominated by fluid flow. The three cases on the diagonal from lower left to top right in Figure 12 show a structure in between the two extremes where there is deviation from the hemispherical shape but not highly directional melting as in the top left melt pool. These images show a clear trend of deepening the weld pool with increased energy density which is to be expected. Increasing the energy density eventually caused keyholing with pores forming in the weld pool. While this area may offer insight into fluid flow of the weld pool it is not the current focus and the model does not account for porosity. Since the weld pools are getting deeper with increasing energy density based on power and velocity, it can be concluded that the surface tension gradient is positive as explained in Figure 3, causing the hotter liquid directly beneath the laser to flow downward causing a deeper, narrower weld pool. A problem seen in steel welding is that the surface tension gradient can change between negative and positive depending on surface active elements, especially sulfur.[26] While the surface tension gradient is expected to be positive for this alloy due to its popularity in welding, it is important to ensure that this particular sample followed this behavior.[26] Preferably, an AM alloy would have a negative surface tension gradient allowing for more bonding between the hatch lines in a given layer while not impacting lower layers as nonuniformly.[10] From these observations, the chosen test matrix seems to cover

all desired testing conditions ranging from an almost perfect hemisphere to obvious keyholing and pore formation.

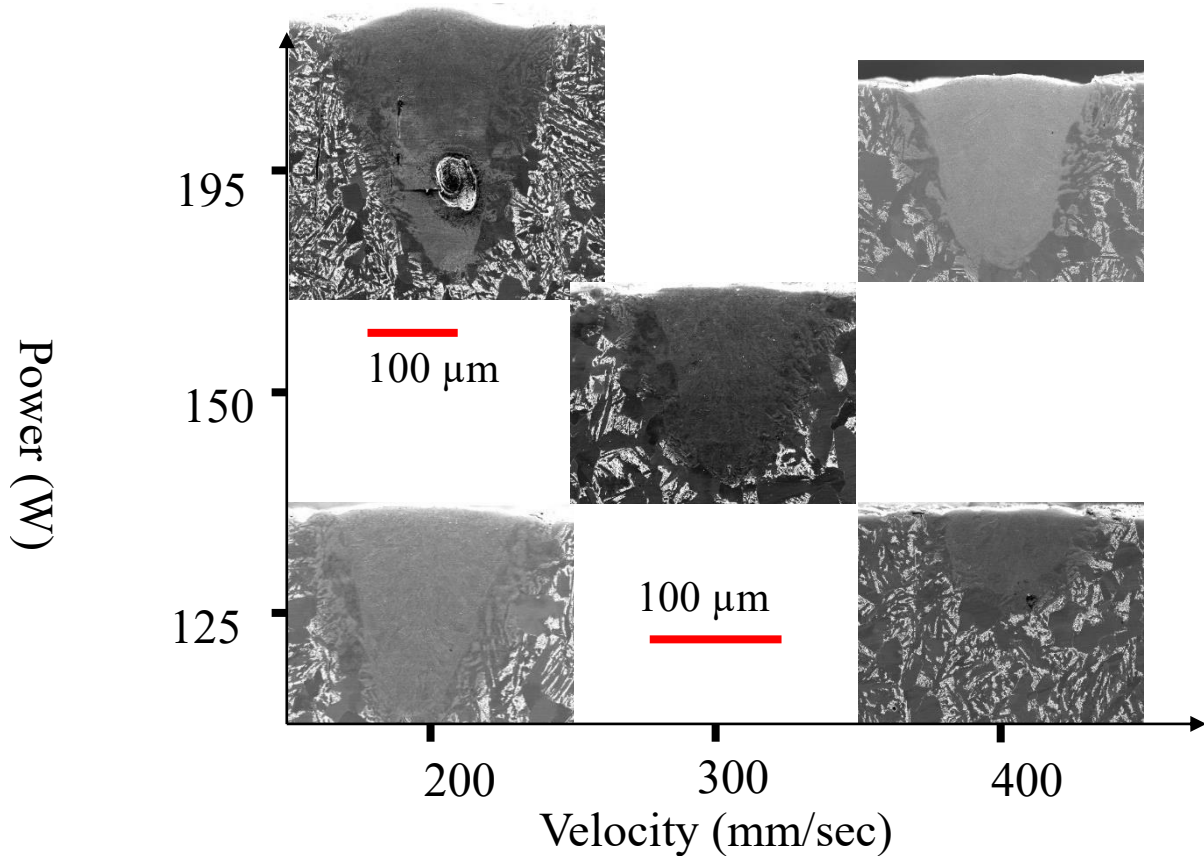


Figure 12: Picral etched SEM secondary images of the weld and surrounding microstructure for the single line laser welds, over ranges of power and velocity.

Vickers hardness data taken with a 0.5kg load with a dwell time of 15 seconds can be found in Table 5. One indent was taken at the center of each single pass for a total of three indents for each parameter set within the test matrix. The Vickers hardness was calculated as per ASTM standard E92-17[66]:

$$HV = 1854.4 * \frac{F}{d_1 * d_2} \quad (3)$$

where F is the force applied in kg and d_x is the length of the indent diagonals in μm . The data from Table 5 shows high hardness corresponding to a high amount of martensite transformation. Comparing these hardness values with the Jominy end quench test data shown in Figure 8, the

expected maximum hardness does not seem to match. The highest hardness from those tests was 474 HV, which is much lower than the lowest value presented here.[67] As of right now there is no apparent reason for this difference. One potential explanation is a super-strengthening effect cause by a drastic increase in the dislocation concentration in martensite, although there are insufficient data at this point to evaluate this hypothesis.[68]

Table 5: Average Vickers hardness measurements of single pass test cases taken at HV0.5 with one indent in each single pass for a total of 3 indents. The variation is the standard deviation of the indents. *400mm/sec/125W was taken at HV0.2 due to the size of the melt pools being so much smaller.

Parameters	Single Pass Hardness (HV)
200 mm/sec 125W	580 ± 7
200 mm/sec 195W	557 ± 54
300 mm/sec 150W	558 ± 3
400 mm/sec 125W*	564 ± 20
400 mm/sec 195 W	596 ± 19
As-received Bulk (normalized)	212 ± 7

Nano-hardness measurements can be qualitatively assessed to see variations caused across the melt pools as shown in Figure 13. The nano-hardness data cannot necessarily be quantitatively compared to the micro-hardness data without having some knowledge of the elastic deformation that occurs in nanoindentation. The nanoindents show a region corresponding to the melt pool, harder than the bulk, which is surrounded by a band with intermittent regions either harder or softer than the melted area. This coarse grid of measurements has some variations due to the small indents being in single phases of multiphase regions; a more highly resolved grid will make clear the small-scale variations in this region.

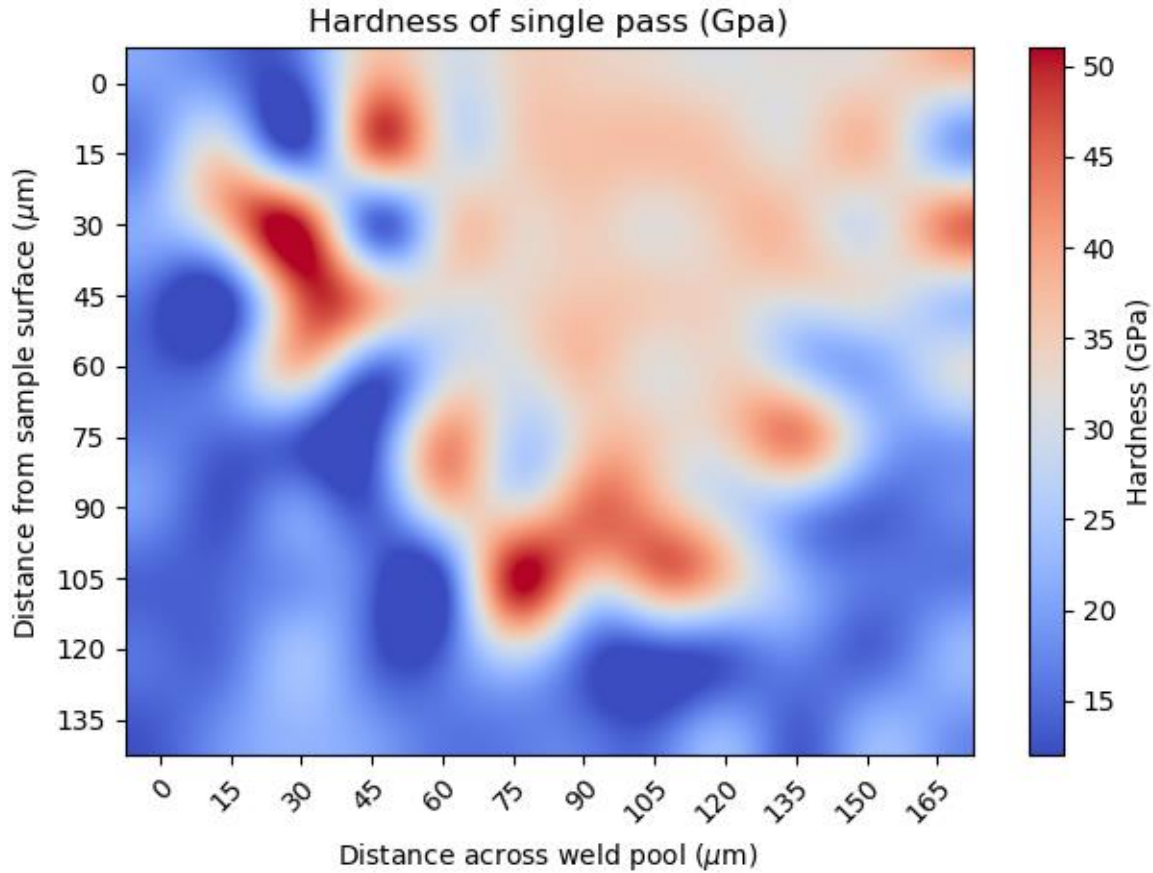


Figure 13: Nanohardness map of single pass 200 mm/sec 125W case. Each tick represents 15 μm for a test space of 180x150 μm .

Comparison of the Vickers hardness values with the hardness values of the Jominy end quench test in Figure 8 show that these hardness values appear to be higher than previously published, as the increased hardness caused by dislocations is already accounted for in the hardness reported for martensite.

2.3.3. Multipass experiments

Moving on to the multi-pass microstructures, a representative section of each set of parameters can be seen in Figure 14. A labeled graphic of the multipass cases can be seen in Figure 15 which has labels for regions that will be discussed. As previously, the highest energy density case, 195W at 200 mm/sec is in a different length scale due to the much deeper penetration of the melt pools making it impossible to image the whole melt pool at a higher magnification. Similar to the single

pass cases, as the energy density increases from the bottom right to the top left, the weld pools grow deeper and less hemispherical. The white streaks in the center of the melt pools correspond to the tempered regions caused by subsequent passes. Looking at the location of the melt pool lines and the tempered regions, shows that there is an overlap region that is retransformed back to austenite and then quenched again to martensite since the tempered region does not sit directly next to the melt line.

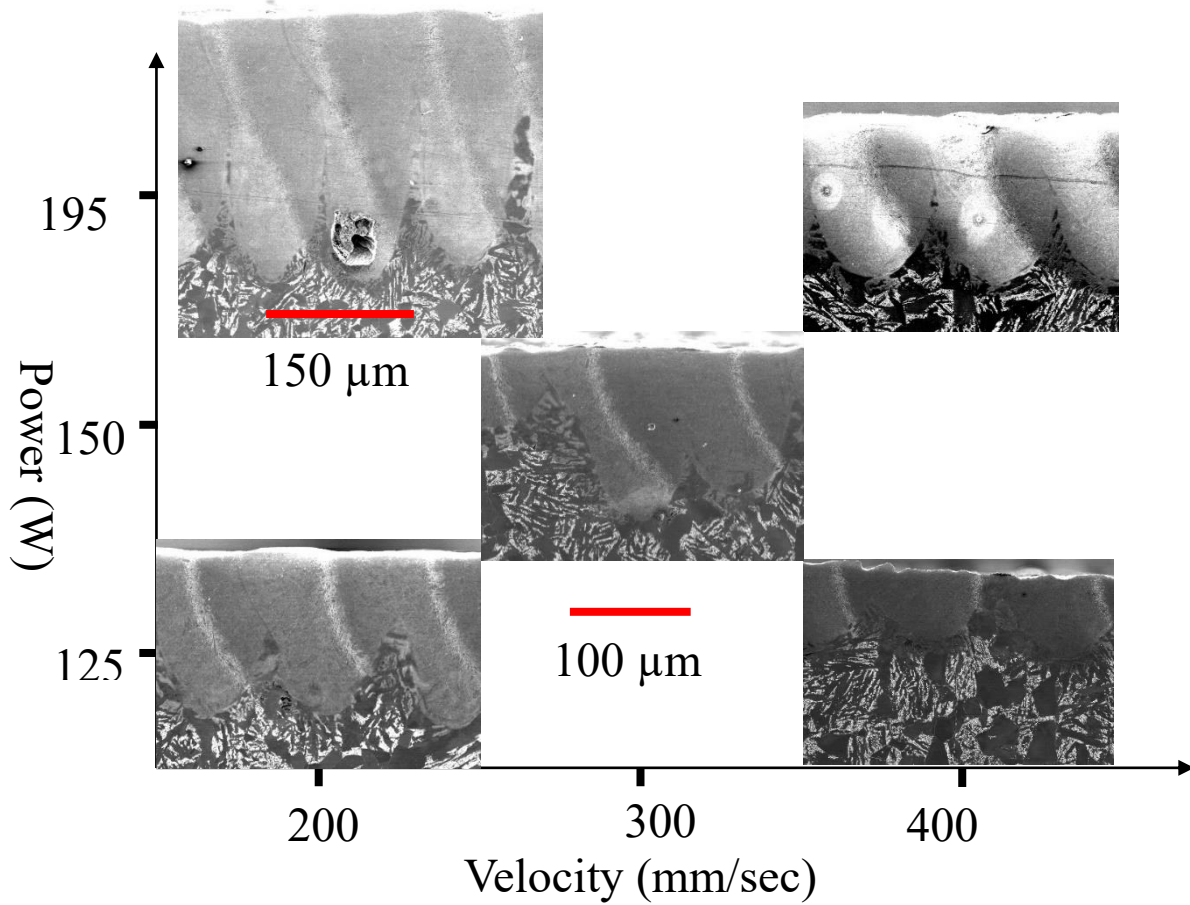


Figure 14: Secondary SEM images of the multi-pass laser welds of the parameters of interest etched with picral showcasing the melt pools and heat treatment of previous passes. The laser alternates between into and out of the page progressing from the left to the right.

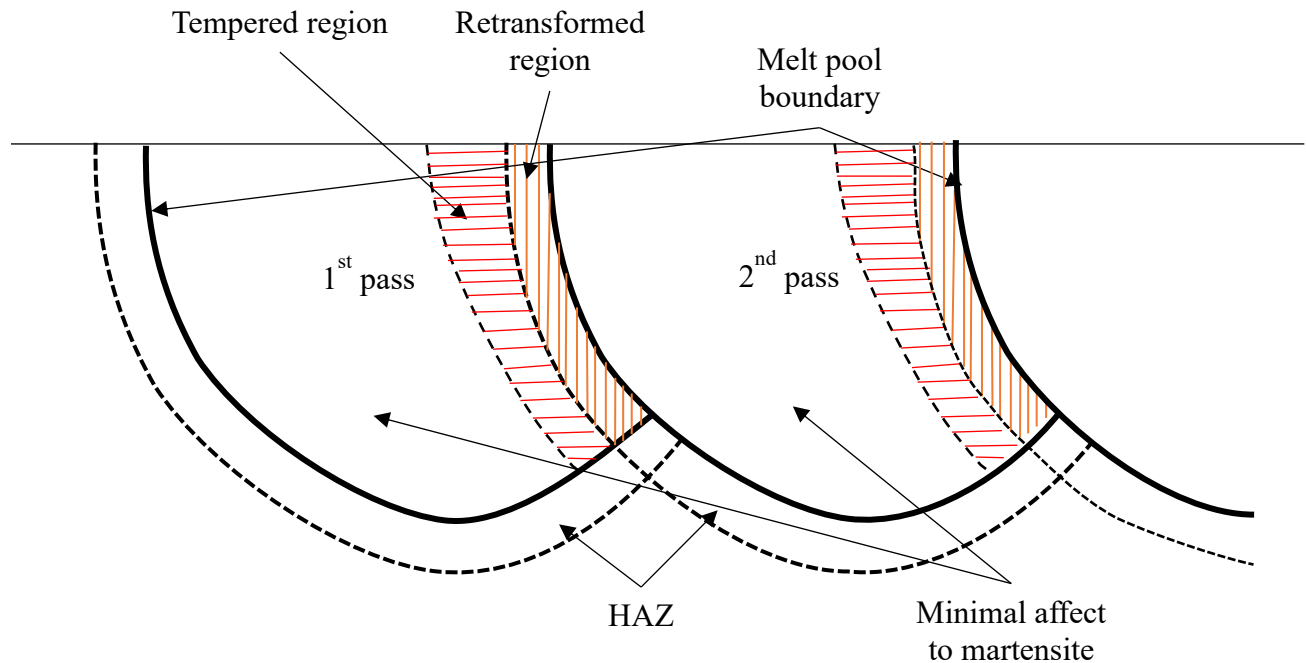


Figure 15: Cartoon graphic of the multipass experiments with labeled regions for simplicity in discussion.

Starting from the lowest energy density case, 125W at 400mm/sec, the weld lines seem to be fairly hemispherical but appear to barely overlap or touch each other. As the speed decreases and power increases the weld pools become less hemispherical and the tempered region extends across more of the weld lines. This is caused by more energy being put into the given location over a given amount of time causing higher maximum temperatures further away from the melt pool. A close up of the white regions and the surrounding area is shown in Figure 16, showing the region that was retransformed on the right of the high carbide area and a gradient decrease of the carbide on the left where the heat was not as intense so less carbide formation could occur.

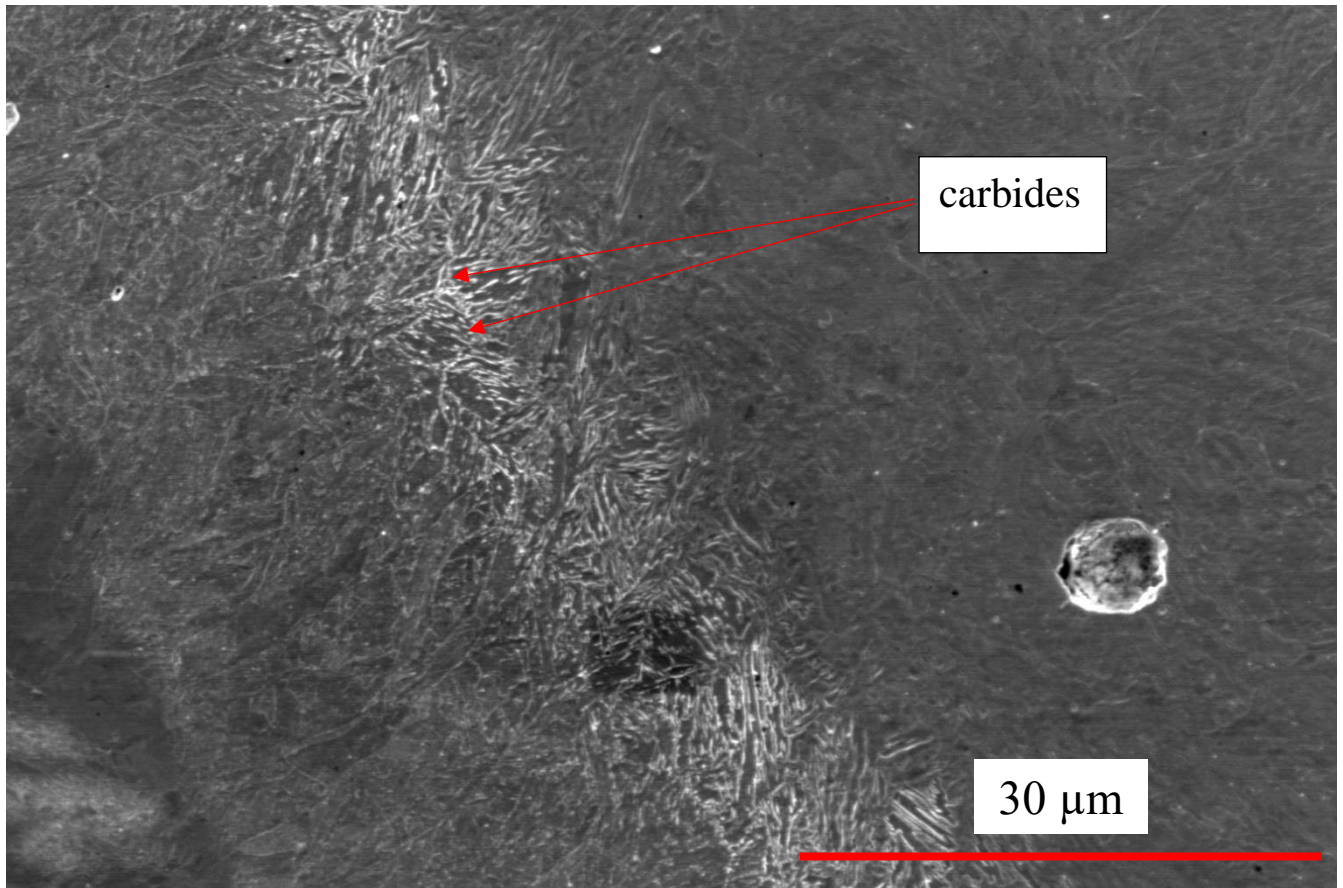


Figure 16: Secondary SEM image of a zoomed in view of the tempered boundary showing increase in carbide amount in the 300 mm/sec 150 W case. The carbides are the white areas where carbon has migrated from the surrounding martensite and come out of solution.

Hardness measurements were also performed on the multi-pass regions to quantify the variations that appear in the micrographs. Microhardness was performed with a load light enough to test just the tempered regions showing carbide formation and complete martensite regions formed from retransformation or not visually impacted by subsequent laser passes, to confirm that tempering did in fact occur. Hardness values of the separate regions can be seen in Table 6. The gathered data shows that there is a significant softening effect caused by the consecutive passes overlapping with each other causing remelting and tempering of the already processed melt pools. All cases except the 2000mm/sec/195W show a slight reduction in hardness from the single pass cases in the visually unaffected region. While the tempered region(white streaks), shows a larger tempering effect across these cases as well. The highest energy case, 200mm/sec/195W appears to have such a large heat affected zone that tempering occurred consistently throughout each consecutive pass.

Table 6: Hardness of multi-pass regions taken with HV0.2. Each section was indented 5 times and variation shown is the standard deviation. Note that in the 200 mm/sec/195W case each melt pool had such a large area of effect there was no difference between zones and the 400mm/sec/125W case had so little interaction between melt pools it was impossible to take measurements.

Parameters	Visually unaffected region hardness (HV)	Visually tempered region hardness (HV)
200 mm/sec 125W	514 ± 15	427 ± 28
200 mm/sec 195W	462 ± 20	462 ± 20
300 mm/sec 150W	542 ± 14	427 ± 23
400 mm/sec 125W	540 ± 51	Low interaction
400 mm/sec 195 W	526 ± 32	442 ± 4

Qualitative nanoindentation measurements were performed on a multi-pass sample of 300 mm/sec 150 W as well. The interpolated contour plot in Figure 17 shows a hardened region that follows the typical melt pool but there is an area of lower hardness(A) in each weld pool which would imply tempering. Based on the images in Figure 14 the tempered region would be slightly away from the melt pool boundary so an approximation of the boundary is given.

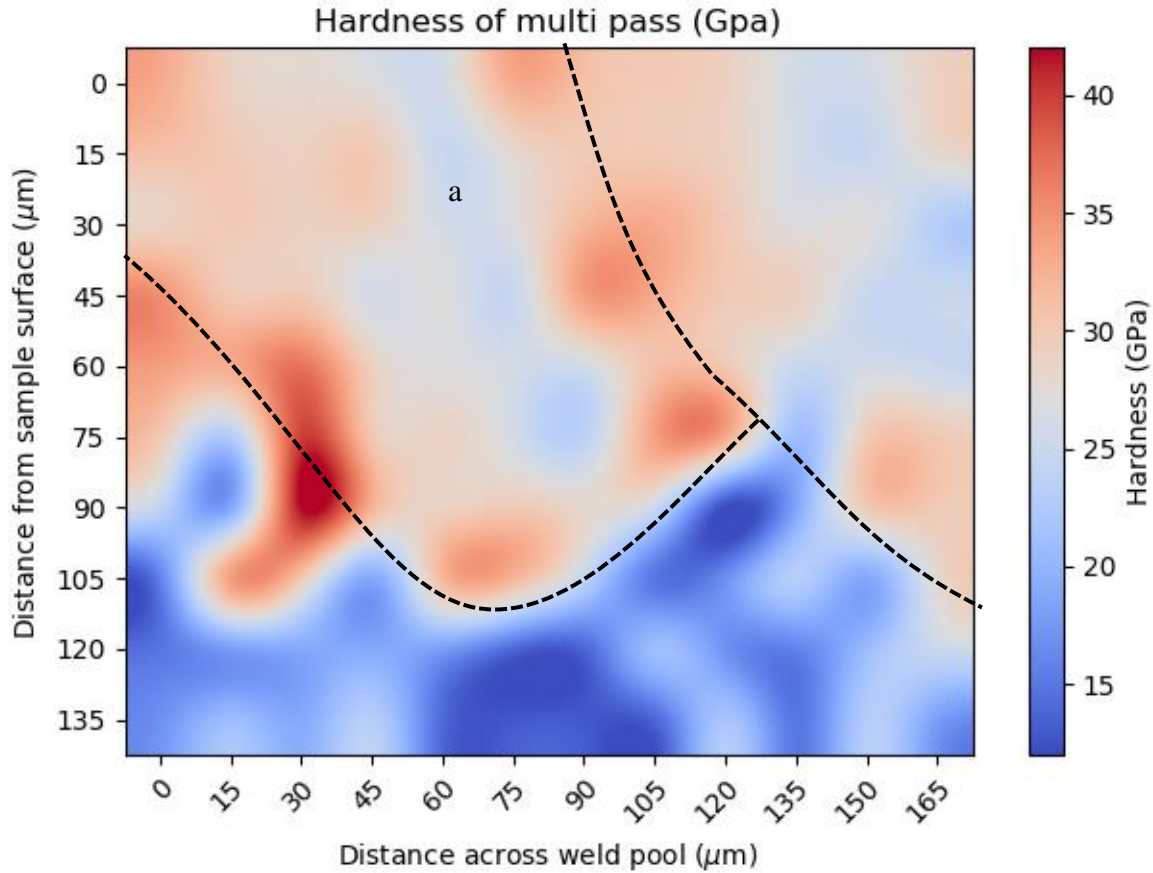


Figure 17: Nano-hardness of the multi-pass region. Melt pool lines are approximated by the dashed lines. The tempered region is shown(A).

2.3.4. Other features of interest

Another feature was found around the outside of the melt pool that was unexpected but not unsurprising. A view of a single pass(300mm/sec/150W) where these features are prominent is shown in Figure 18 with a zoomed-in view of a prime example shown in Figure 19. Looking outside the weld line there is clearly some uniform transformation to martensite where everything heated up, transformed to austenite, and quenched. But further away from the melt pool, the metal is not entirely martensite. things become less consistent depending on the grains and grain size. The diffusion rate of carbon is fast enough that the pearlite lamellae can diffuse carbon across each other quickly enough for austenitization to begin.[69][70] But this is not the case for the large carbon-lean ferrite grains. Since the temperature required for ferrite transformation to austenite is

extremely high(at low carbon content), it does not to transform to austenite, and so it cannot quench to martensite. There are some large ferrite grains that surround the melt pool but martensite penetrates further following the pearlite grains until the temperature is too low for austenitization to occur anymore. This can cause inconsistent pinning and edge effects due to these large grains creating an inconsistent layer around the outside of the weld pool. At the edge of the heat affected zone there appears to be partially transformed pearlite where the temperature was high enough for austenitization but for a time less than necessary for the carbon to diffuse far enough to effect the transformation.

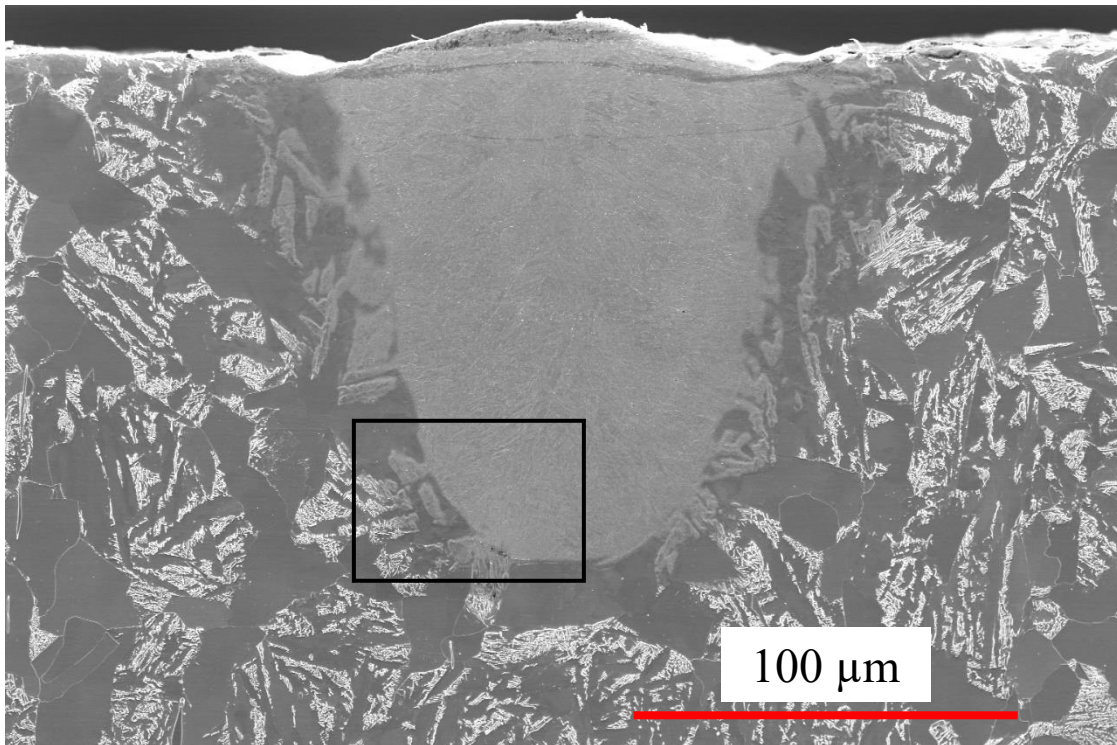


Figure 18: Single pass where variations outside the melt line are clearly visible. Closeup region is outlined in black square.

HAZ

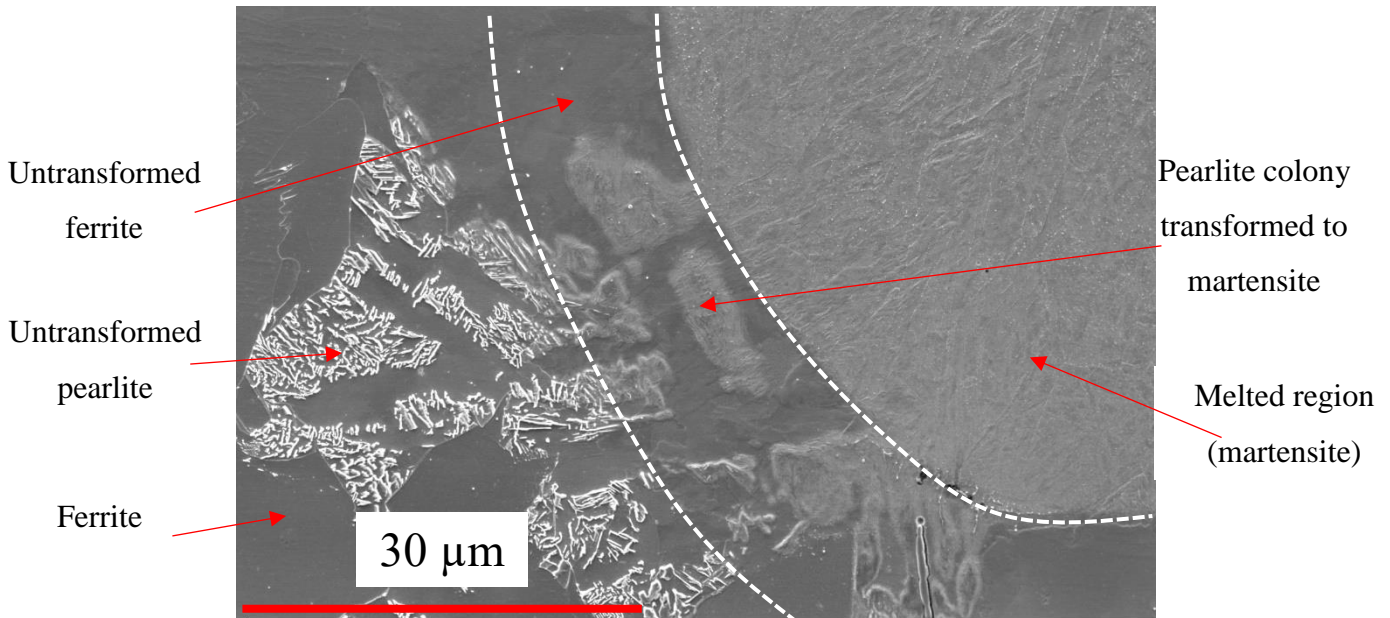


Figure 19: Close-up of features outside melt pool showing partial transformation of pearlite with minimal impact to ferrite.

Due to this variation in edges a deeper weld pool is not ideal as it can cause pockets of untransformed regions causing microstructural variation and, in powders, leave areas that are unmelted porosity. This microstructural variation provides another reason for a negative surface tension gradient for the alloy that is not directly related to the melt pool and porosity formation from keyholing. The negative surface tension gradient allows the pool to spread wider instead of deeper so it would allow a more consistent depth across all regions.

2.3.5. Summary

Within the single pass tests, the shape of the melt pool can be established, which suggests the sign of the surface tension gradient with temperature. Imaging also allowed visualization of edge phenomena showing solid-solid phase transformations in the HAZ directly outside the melt pool. Microhardness measurements of the single passes and one of the multipass cases appear to be uncharacteristically hard without a good explanation. Nano-hardness data qualitatively shows higher hardness regions outside the melt pool in the HAZ. This could correspond to the solid-solid transformation regions as the martensite would have been formed with the local equilibrium C content, which in austenite formed from pearlite in a hypo-eutectoid steel is 0.76 wt %. Inside the melt pools, complete martensite formation occurs, but introducing subsequent passes causes tempering due to thermal interactions. Outside the melt pool a heat affected zone exists with solid-

solid phase transformations caused by the short heating times limiting transformations to the pearlite colonies due to limited carbon diffusion. Being able to match this data with a model would be greatly beneficial so that future work can be investigated without the need for many experiments.

3. MODEL

Modeling of the AM process can provide valuable insight into the process without having to perform an exhaustive number of experiments. It also allows for visualization of data that may not be possible to directly observe in experiments. This allows for correlation of information between the experiments and model once it is calibrated and can offer insight into the process and material responses in domains that have not been experimentally performed. This process starts with understanding the analytical models for the given process starting from a laser melting standpoint. The Rosenthal equation for laser hardening has been shown to be able to accurately predict thermal fields and can be used to validate transient solutions and models. This model can be expanded to include melting if desired by including the latent heat of transformation but if a quantitative analysis is all that is required then any value above the melting temperature can be assumed as the substrate melting. Since this process is so similar to welding, just on a smaller scale investigating the validity of this model would be useful to confirm the accuracy for the thermal model. Other models created by various groups will then be used to evaluate the phase fractions which can then be compared and validated against the experimental results found.

3.1. Analytical and Thermal Models

Laser welding and hardening have long been treated by an analytical model for calculating the temperature profiles of welds outside of the melt pool attributed to Rosenthal.[71][72] The Rosenthal equation assumes the heat source is a point source and that the temperature is calculated based on the distance away from the point. This allows tracking of the heating and cooling of a point based on the laser velocity and distance away from the point. The beam location can be used to calculate the temperature history of a single laser pass.

$$\frac{2 * \pi * (T - T_0) * k * R}{Q} = \exp \left[\frac{-V * (R - x)}{2 * \alpha} \right] \quad (4)$$

Where T is the temperature at that location, T_0 is the temperature before welding, k is the thermal conductivity of the piece, R is the radial distance away from the point source that is being evaluated in three dimensions, V is the laser velocity, α is the thermal diffusivity, x is the distance in the

direction of the laser (note that the laser travels in the negative x direction), and Q is the energy input.[72] The geometry and path of the laser can be seen in Figure 20

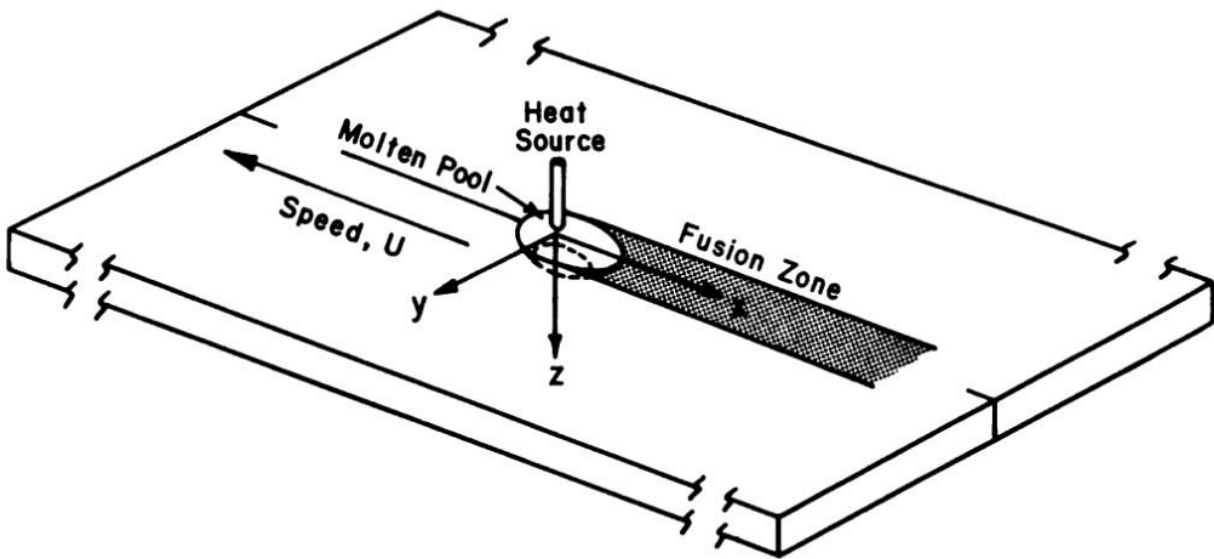


Figure 20: Coordinate system of Rosenthal's solution as it moves with the heat source.[72] An analysis of each plane is shown in Figure 21 centered around the heat source. There is good agreement in the shape of the melt pool with experimental results for welding with a symmetrical weld along the y -plane, and a tear drop shape in the z - and x - planes showing the motion of the laser into an unheated sample while the passed area is cooling.

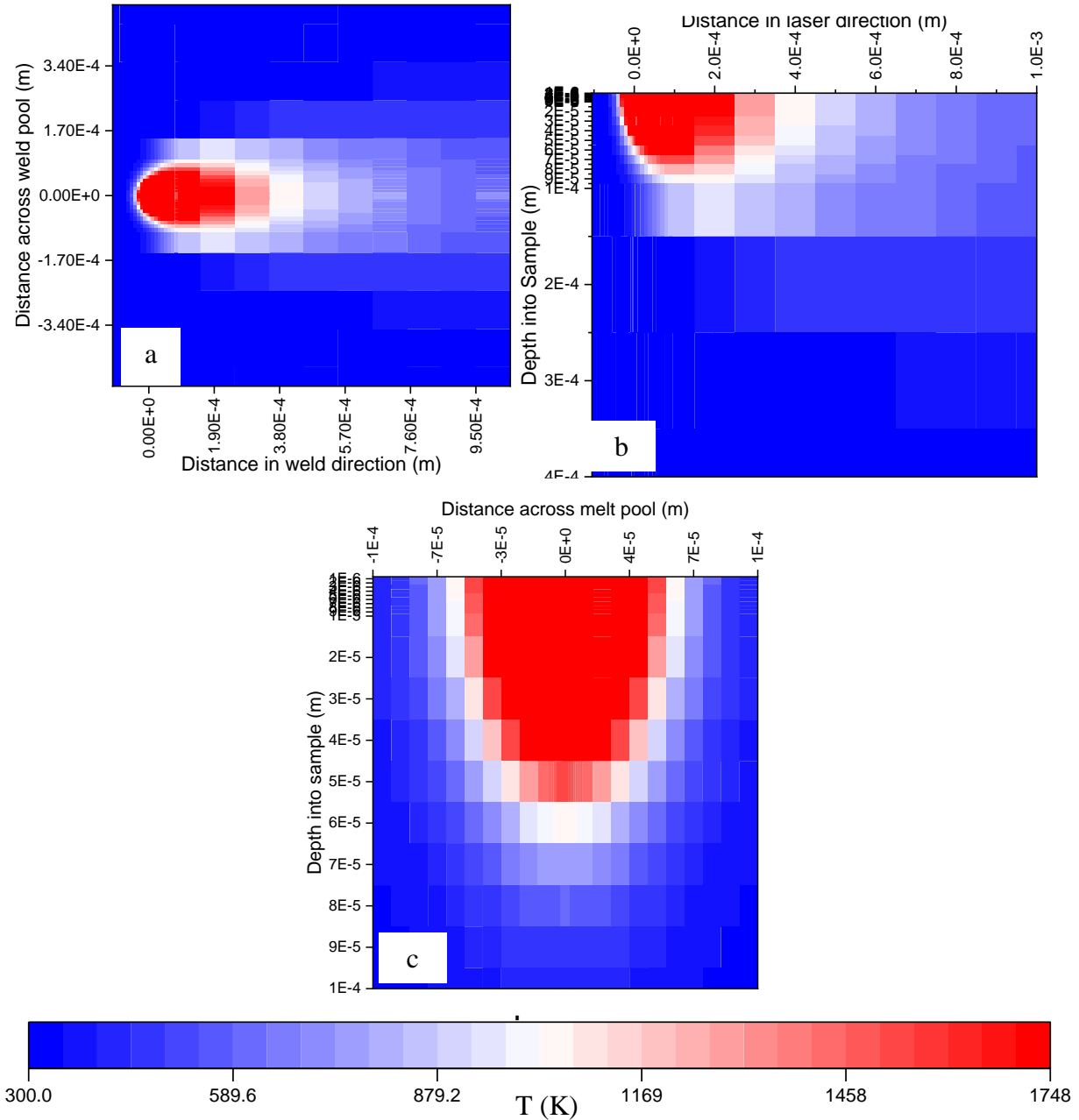


Figure 21: Graphical solutions of the Rosenthal equation across all planes: the z-plane(a), (x-plane(b), and the y-plane(c). Parameters used were 0.4m/s and 195 W.

While the shape of the melt pool as well as the areas that melt are fairly accurate with a width of $\sim 100\mu\text{m}$ and a depth of $\sim 80\mu\text{m}$, the Rosenthal model does not consider fluid flow which can alter the shape of the weld pool. Since the equation assumed that the laser is the origin at all times, without including thermal transport it is not possible to correctly perform analysis on multiple passes. By including heat conduction, a rough estimate of the overall heating can be obtained

which can be used to calculate a multi-pass system similar to a single AM layer. Two passes were done and compared with the thermal model used to show that this equation is still applicable to this process and the results can be seen in Figure 22.

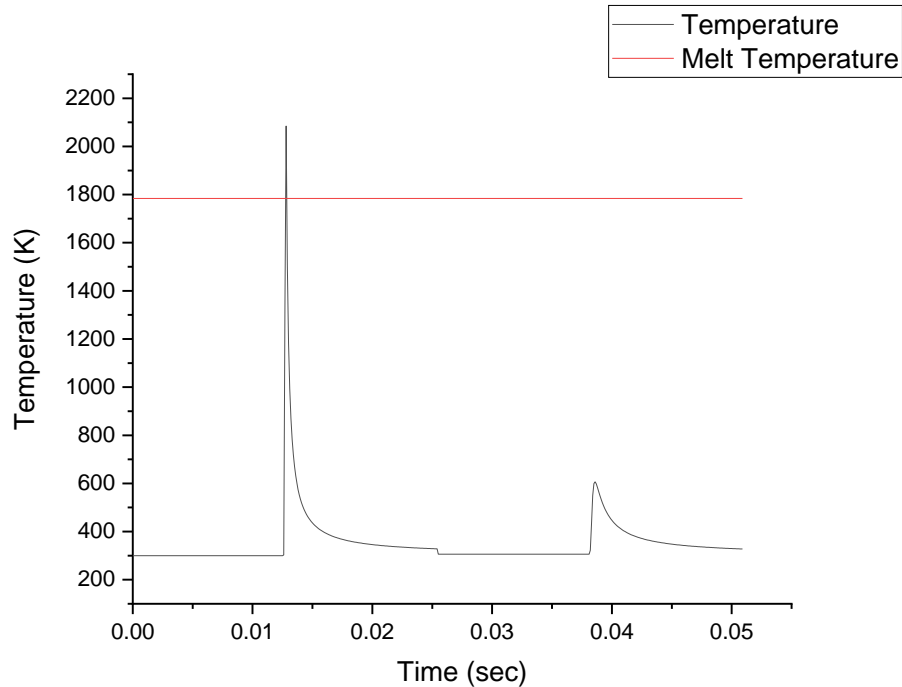


Figure 22: Rosenthal’s equation plus conduction for 2 laser passes at 0.4m/sec, 195W, and 100 μm spacing.

Values above the melting temperature T_m are unphysical as latent heat was not considered. Figure 22 can be compared to temperature over time plots of the single and multi-pass cases of the thermal model created by Coleman et al shown in Figure 23 and Figure 24. While the temperatures do not line up exactly as was expected, the cooling time of ~ 0.005 sec matches extremely closely. This supports the Rosenthal welding analytical equation as an analytical solution to the AM problem being able to more closely link AM with welding. As mentioned earlier without a full inclusion of thermal transport equations though, the Rosenthal equation falls short in calculating the remaining heat at a given location away from the laser so it is important to have a fully capable thermal model as the basis for calculating phase transformations that are sensitive to the time spent in various temperature regimes.

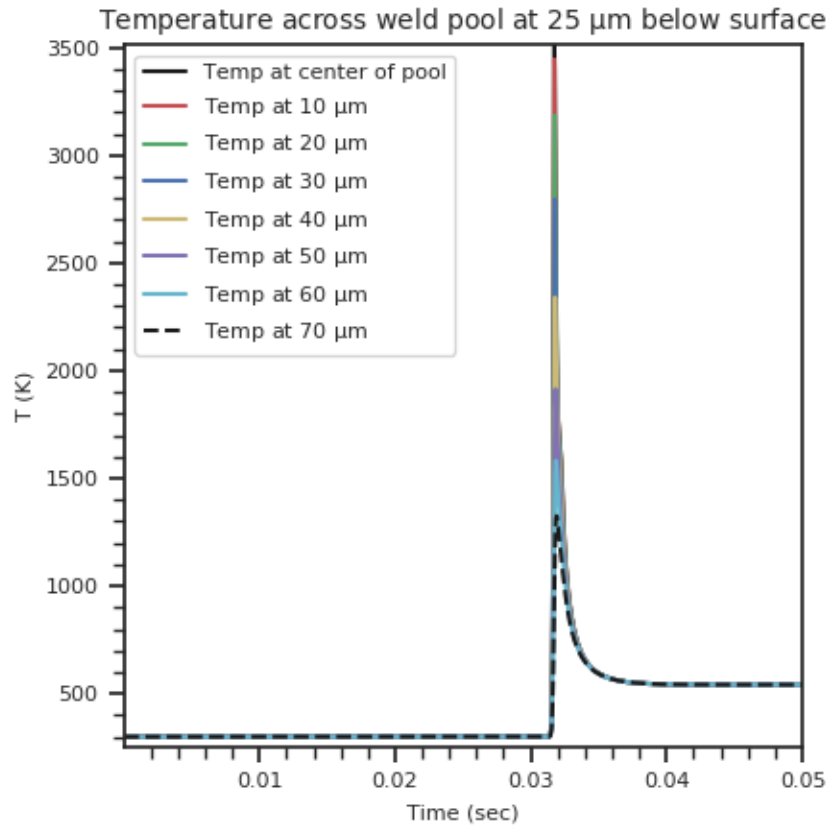


Figure 23: Time versus Temperature plots for a single pass of 400mm/sec and 195W in the Numerical Model. The distances of the legend are μm steps away from the center of the melt pool where probes were placed in the y-direction.

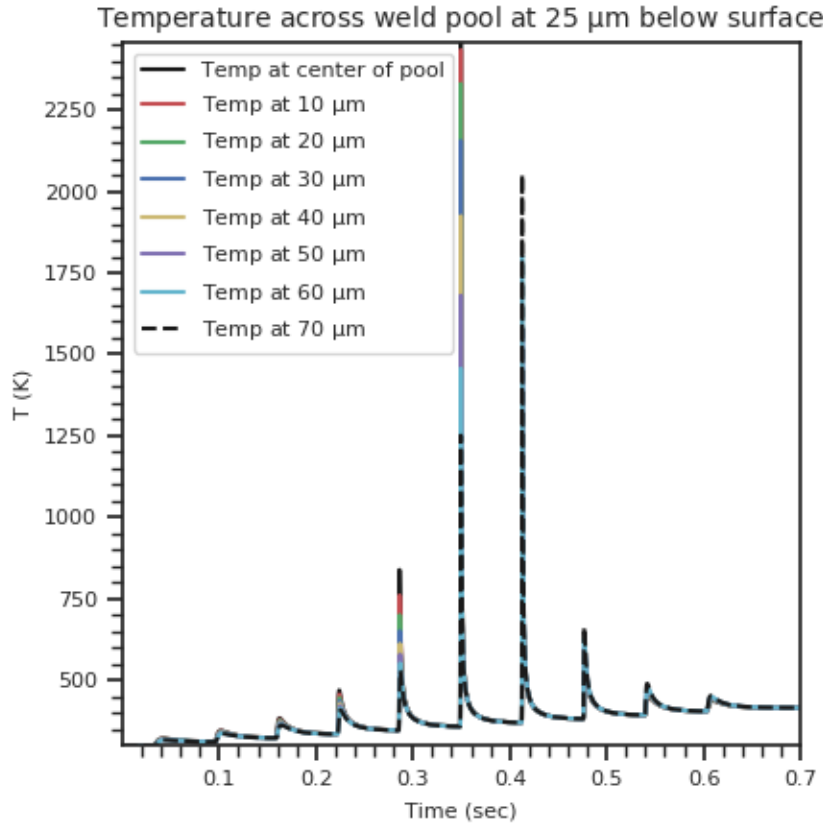


Figure 24: Time versus Temperature plots for multiple passes of 400mm/sec and 195W in the Numerical Model. The distances of the legend are μm steps away from the center of the melt pool where probes were placed in the y-direction.

3.2. Numerical Model

This model was built on the backbone of the thermal model created by Coleman et al. for laser melting. This finite volume model uses a volumetric heat source to heat up the test geometry and can track both solid and liquid phases as well as their interfaces and velocities. The laser, scan path, and test piece can both be manipulated for larger or smaller sizes as well as more or less passes.[10] Constant values for required thermophysical properties were used due to lack of available temperature dependent information on the alloy and are presented in Table 7 as gathered by Sung et al.[73] The thermal emissivity of the top surface was also approximated from IN 625 due to lack of available information on AISI 8620. There are some variables that must be calibrated using experimental data for the material which are shown in Table 8. The most

important system variable required is the absorptivity which is currently not well known for many materials but can be estimated within certain ranges. Most AM models assume that metals have an absorptivity of ~35% for Nd-YAG lasers.[74] This value can change depending on the surface preparation conditions in experiments so it is effectively a calibration factor. Taking this initial estimate and the single pass experiment that was the most hemispherical in shape, a binary search algorithm was used to find the minimum error in the model shape versus the experimental. This was calibrated assuming no fluid flow to eliminate variation in shape that is caused by the Marangoni flow effects in convection dominated regimes and was matched to the most hemispherical test case.[10] The error in absorptivity came to a minimum at 0.3 by using a binary search algorithm that varied the absorptivity across a range looking at comparison of melt pool data to values taken from the experimental samples. The surface tension gradient and absorptivity were both calibrated using the same test case. The surface tension gradient for measuring flow was also fit as closely as possible by best fit as steel tends to have a very large range for surface tension gradient and is explained further in Section 3.2.5.[26]

Table 7: Thermophysical properties of AISI 8620.[73]

Property	Value
Thermal Conductivity ($\text{K}^{-1}\text{m}^{-1}\text{s}^{-1}$)	30.7
Solid Density (kg m^{-3})	7367.0
Liquid Density (kg m^{-3})	7029.0
Solidus Temperature (K)	1634
Liquidus Temperature (K)	1784
Solid Specific Heat ($\text{kg}^{-1}\text{K}^{-1}$)	669.4
Liquid Specific Heat ($\text{kg}^{-1}\text{K}^{-1}$)	778.2
Viscosity (N s m^{-2})	0.00535

Table 8: Properties that required experimental calibration.

Property	Value
Emissivity	0.13
Laser Absorption	0.3
Surface Tension Gradient($\text{N/m}^*\text{K}$)	6e-4

These material properties create the weld lines overlaid in Figure 25 where there is clearly not as much similarity between all the other cases as with the model case used to calibrate. This can be caused by a couple different reasons. The surface of the melt pool could have been depressed due to the laser power or could have been vaporized by the high energy density. The vapor would alter the absorptivity as would the dip in the surface allowing the laser to bounce around inside the depression allowing a higher energy transfer into the melt. This is not accounted for in the model as the model assumes there is no material loss and there is no change in the height of the surface which is valid in the conduction or non-flow dominated regime.[10] Once the material properties for the thermal model are determined, the phase transformation numerical model can be

considered. While there are not many new properties that are required for the phase transformation model, the equations commonly used must be investigated due to the rapid transformation times seen. Historically, the austenite transformation has been seen as completely instantaneous but in this process that is not the case. Martensite tempering has historically been modeling by the Johnson-Mehl-Avrami-Kolmogorov (JMAK) equation but this assumes that the phases are in equilibrium which martensite and tempered martensite are not considered equilibrium phases. Understanding the basis for historical models used as well as investigating alternatives that may potentially fit this process occurring on such a small timescale is in order.

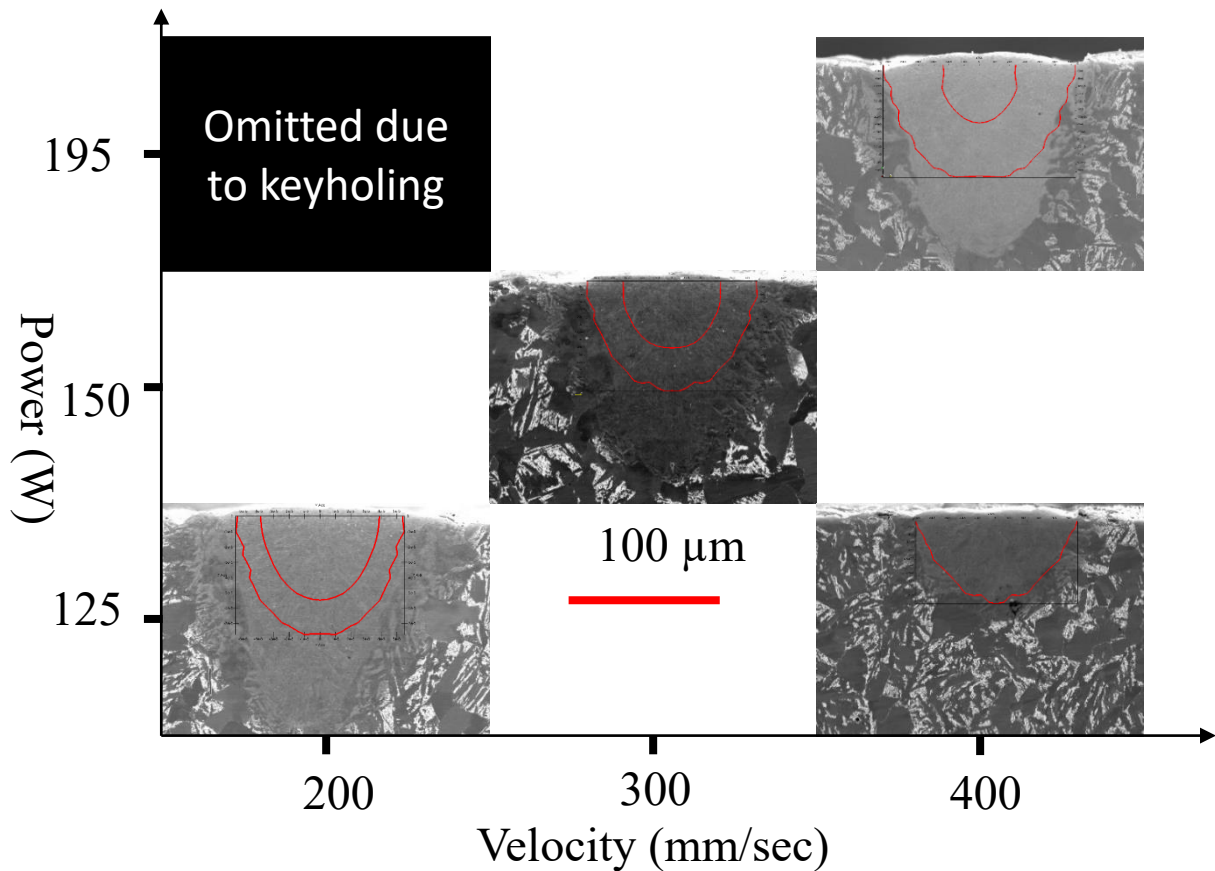


Figure 25: Model weld lines overlaid on experimental weld lines in red. In case of double line, the outer red line is the full melt pool

3.2.1. Diffusional Transformation (JMAK)

Historically, steel transformation models have been governed by a few different equations depending on the phases being formed. The diffusional phase transformations of ferrite, pearlite, and bainite have been predicted using the JMAK equation.[75]

$$f_i = f_i^{max}(1 - \exp[-b_i * t_i^n]) \quad 5$$

Where f_i^{max} is the maximum volume fraction of the phase i , b_i and n_i are temperature-dependent parameters for the given phase, and t is time elapsed for solving the volume fraction of the given phase at that time f_i . [76] But since this is not an isothermal process, Scheil's additivity principle must be taken into account. When assuming continuous cooling this condition must sum to 1 for the transformation to occur. [76][77]

$$\int_0^t \frac{dt}{t_a(T)} = 1 \quad (6)$$

Where $t_a(T)$ is the time needed to reach the volume fraction f_i in the isothermal transformation. Given the known finite time increments and changes in temperature this can be used to calculate not only the phase transformation itself but also the incubation time prior to the transformation if the Continuous Cooling Transformation (CCT) diagram is known. This simplification of the integral into a summation. [4][5]

$$\sum_{i=1}^n \frac{\Delta t_i}{\tau_s(T_i)} \approx 1 \quad (7)$$

For the incubation time, Δt_i is the calculated time step change and $\tau_s(T_i)$ is the time required for transformation to begin at the temperature at time i . This process is summarized in Figure 26 showing how calculating the incubation time would fall on a CCT diagram.

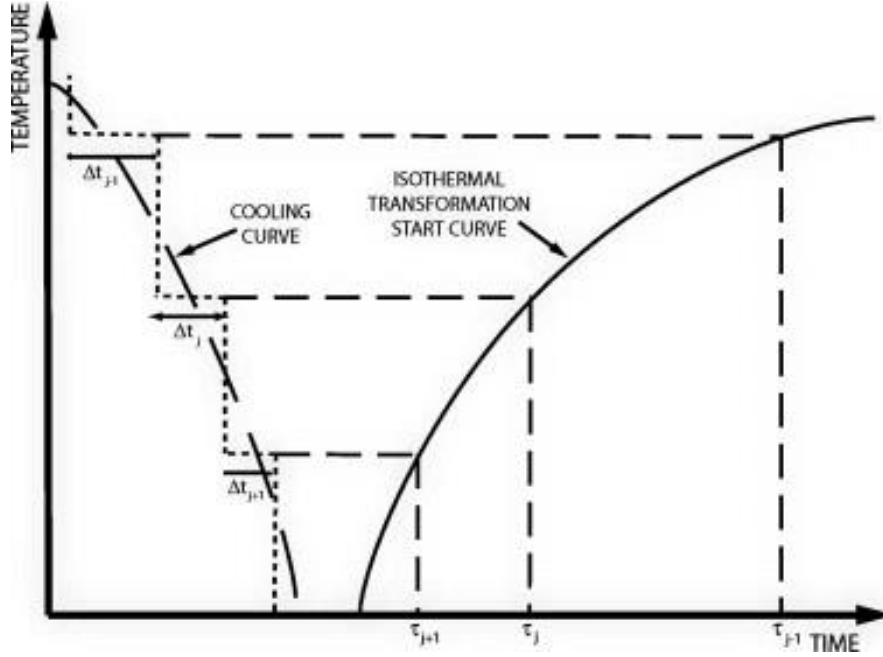


Figure 26: Calculation of anisothermal incubation time found by using Sheil's additivity principle.[77]

While calculating the transformation percentages after formation has begun follows effectively the same concept but transformation start times and rates vary by temperature and time it is important to correctly follow the isochores of the CCT diagram. This requires the calculation of a fictitious time step to represent the time needed to transform the actual amount of f_i at the end of time t_i . The fictitious time step t_{i+1}^* represents the time needed to transform f_i at the end of time step t_i :

$$t_{i+1}^* = \left[-\frac{\ln(1 - V_i)}{b_{i+1}} \right]^{\frac{1}{n_{i+1}}} \quad (8)$$

The fictitious time is then used to calculate f_{i+1}^* , a fictitious transformed volume fraction.

$$f_{i+1}^* = 1 - \exp[-b_{i+1}(t_{i+1}^* + \Delta t_{i+1})^{n_{i+1}}] \quad (9)$$

The new volume fraction is then calculated by also including the maximum possible transformation amount as well as the volume fraction of austenite that is available. The maximum transformation amount is important in cases where the total transformation will not equal 1 and can be found using lever rule in the two-phase regions.

$$f_{i+1} = f_{i+1}^* * (f_i + f_\gamma) * f_{i+1}^{max} \quad (10)$$

temperature is set where the first measurable amount of martensite is found. T_{KM} is dependent on alloy composition can be calculated.[70]

$$T_{KM}(^{\circ}C) = 462 - 273x_C - 26x_{Mn} - 16x_{Ni} - 13x_{Cr} - 30x_{Mo} \quad (12)$$

In the initial paper by Koistenin and Marburger α was taken to be 0.11 but that is only applicable to plain carbon steels around the eutectoid composition.[78] But more recently van Bohemen and Sietsma were able to also modify this value based on composition.[70]

$$\alpha = 0.0224 - 0.0107x_C - 0.0007x_{Mn} - 0.00005x_{Ni} - 0.00012x_{Cr} - 0.0001x_{Mo} \quad (13)$$

By modifying these parameters van Bohemen and Sietsma were able to expand the Koistenin-Marburger equation to alloy steels as well as steels further away from the eutectoid composition.

3.2.3. Austenitization and Tempering

Austenitization in the past has been assumed to be instantaneous as the transformation to the austenitic phase begins once the temperature is high enough for it to be stable. The transformation happens on shorter time scales as compared to most processes so if the temperature field exceeds the austenitization temperature it is assumed to be austenitized. But this is not true in the AM processing regime. As noted by Orazi et al. and Fortunato et al. in laser hardening austenitization happens on the order of microseconds for laser hardening.[8][9] They show that this is important in accurately predicting laser hardening tempering in multi-pass cases which typically uses a wider and slower laser beam. It stands to reason that a smaller, faster laser as found in AM processes would run into similar issues if following the assumption that all heat-affected material transforms to austenite. In this model, time steps are taken on the order of microseconds so Fortunato et al's assumptions are followed. Calculating the transformation to austenite uses the integral transformation time that Fortunato et al. propose for rapid transformations[18], [34], [79], [80]:

$$I_x = \int_{t_{start}}^t \exp\left(-\frac{Q_x}{RT(t)}\right) dt \quad (14)$$

where I_x is the time it takes for the transformation to take place, t_{start} is the time required for the transformation to begin and the entire equation is governed by an activation energy Q_x that is related to the transformation. Q_x can be considered a material constant based on the material being treated by the laser and is structure dependent so it will differ in cases such as ferrite to austenite

and martensite to austenite. Once the integral transformation time is found it can be used to calculate the total phase formed up to that point using:

$$f_x = \frac{I_t - I_{t,min}}{I_{t,max} - I_{t,min}} \quad (15)$$

where f_x is the proportion of the phase transformed in the nonequilibrium regime. This can be multiple by a scaling factor for two phase regimes to account for a reduced driving force based on lever rule at that temperature. Once f_x reaches 1 it has effectively all transformed under the assumption that it is in a single-phase region. If it is not in a single-phase regime it effectively follows the equilibrium calculations of those phases, in this case the only two-phase region would be ferrite-austenite. Tempering under such rapid thermal cycles is also assumed to follow these equations as there is little time for carbon to diffuse out of the martensitic matrix. These equations assume a distribution of transformations due to local compositional variation and grain size which would have a statistical distribution of transformations as shown in

Figure 28 [79]:

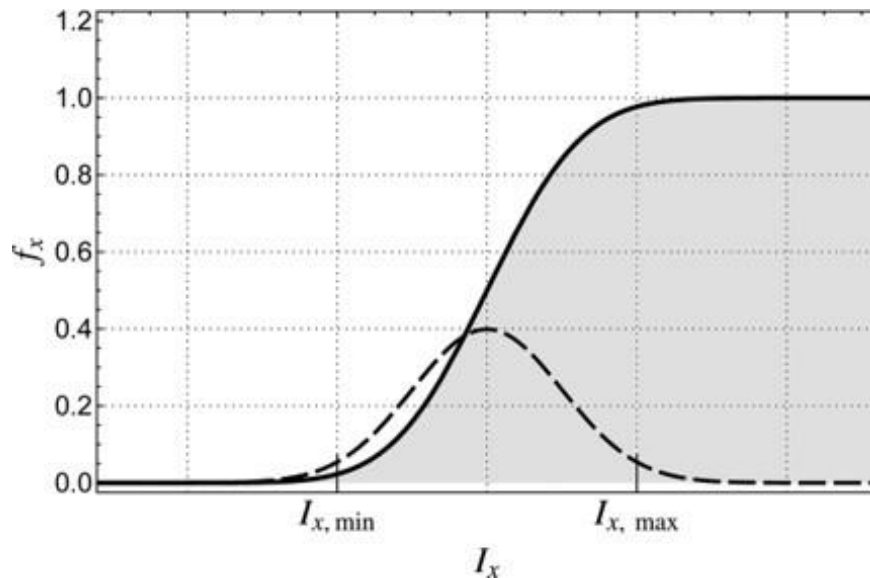


Figure 28: Statistical distribution of I_x transformation. The dashed line showing phase transformed at the individual time and the solid showing cumulative transformation.

For simplicity this distribution can be approximated by a linear fit between I_x and f_x for both stable and unstable phase transformations in steel so it is applicable for both austenitization and tempering. The linear approximation can be seen in Figure 29 [79]:

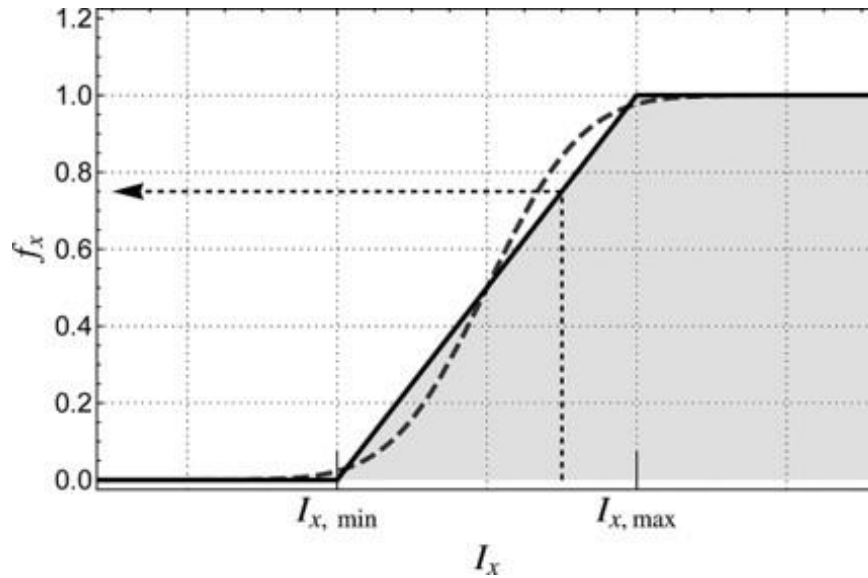


Figure 29: Linear approximation of f_x allowing for model simplicity.

The question arises of if austenite and tempering phases are formed by diffusion similarly to ferrite, pearlite, and bainite then why a different set of equations instead of just the JMAK equations? This is due to the fact that for the phases that are modeled by the JMAK equations can only be formed by diffusion within a certain temperature range but austenite and tempered martensite can also be formed solely by temperature. Austenitic changes are caused by the crystallographic change from BCC to FCC once the local composition is stable in that phase. And tempered martensite has increased kinetics of occurrence as temperature rises due to changes in solubility of carbon and the energy of the atoms. One issue to note with this model currently is that martensite and tempered martensite are technically not separate phases but simply a change in crystal structure from the former to the latter but are currently calculated as two completely separate phases. This can cause issues when calculating mechanical properties to compare with experimental results.

3.2.4. Hardness Calculation

With few experiments to compare data too, without doing a large destructive test, hardness is the easiest property to model and compare to experimental results. Equations for calculating Vickers hardness of AISI 8620 steel was found in the ASM Heat treating handbook Vol .4 of ferrite/pearlite and bainite [81]:

$$HV_B = 323 + 185C + 330Si + 153Mn + 65Ni + 144Cr + 191Mo + (89 + 53C - 55Si - 22Mn - 10Ni - 20Cr - 33Mo) \log(\dot{T}) \quad (16)$$

$$HV_{FP} = 42 + 223C + 53Si + 30Mn + 813Ni + 7Cr + 19Mo + (10 - 19Si + 4Ni + 8Cr + 130V) \log(\dot{T}) \quad (17)$$

where the element names in the equation are weight fractions of the given element and \dot{T} is the cooling rate. The ASM handbook also has an equation for calculating hardness of martensite as well but these equations are for if there is a mix of phases present during formation which is not true for the martensitic formation. It is well known that pure martensite hardness is governed heavily by the carbon content and as such is written with carbon being the only elemental effect as shown in Equation 1:[22]

$$HV_M = 884 * C * (1 - 0.3 * C^2) + 294 \quad (18)$$

For calculation of tempered martensite hardness a method was created by Fortunato et al and was used in this work for calculating the total hardness of the martensite and subsequent tempering of the location[34]:

$$H = f_m [f_h (H_m - H_b) + H_b] + (1 - f_m) H_b \quad (19)$$

where H is the overall hardness of the martensitic region taking into account martensite and tempered martensite. H_m is the hardness of the pure martensite which is calculated above in Equation 18. H_b is the hardness of the bulk material which can be found in Table 5. f_m is the fraction of martensite and f_h is the tempered martensite fraction as given by Equation 20:

$$f_h = \frac{\text{tempered martensite}}{\text{total martensite volume}} \quad (20)$$

3.2.5. Fitting surface tension gradient

There is high uncertainty in the surface tension gradient of steel as it is generally a function of surface active elements, in steel's case typically oxygen and sulfur.[4][5] Keene et al. assumed that in an atmosphere with low oxygen content, oxygen can be neglected as an active element which leaves only sulfur. This assumption can be considered since the AM build chamber was pumped with N₂ gas prior to the build. The issue arises in determining the surface tension gradient

as a function of sulfur content as most steel specifications, AISI 8620 included specify a maximum sulfur content only of 0.4 wt%. While this is generally low when considered as an impurity in steel it causes many problems for the surface tension gradient, as Keene et al, and Pinkerton and Li note, sulfur causes the surface tension gradient of steel to fluctuate from negative to positive at ~0.1wt% which is well within the limits of the specification.[26], [74] Additionally, since the laser goes over such a small area in a given pass that means that the surface tension gradient can vary drastically over a small region with varying sulfur content. Since the experiments became narrower and deeper with increasing power it is apparent that the surface tension gradient is positive so some values within the ranges of Pinkerton and Keene's groups were tried and the resulting melt shapes from the model are overlaid in Figure 30 in red.[26], [74] The tested surface tension gradients were $2e-4$, $4e-4$, $6e-4$, and $8e-4$ showing an increase in penetration as the value increases. As can be seen in Figure 30, the $6e-4$ surface tension gradient fits the shape and size of the weld pool the best so this value was used to model the flow for the other parameters in the experimental matrix.

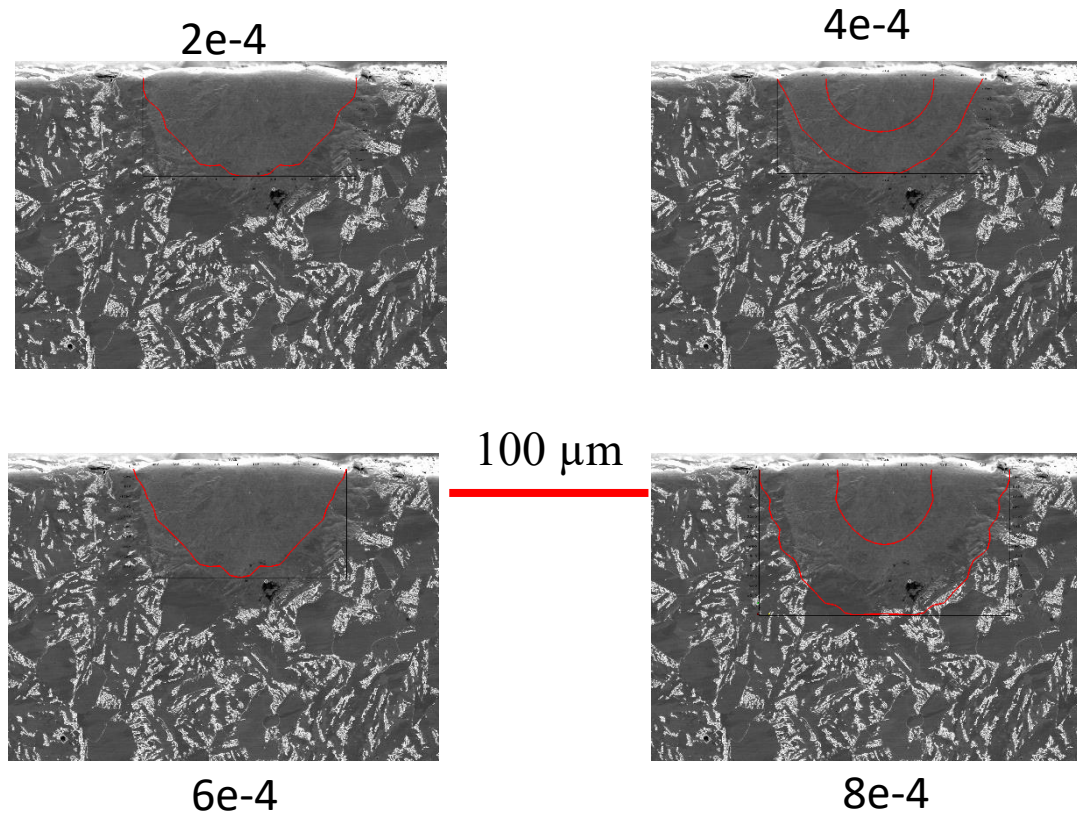


Figure 30: Overlay of modeled melt pool size in outer red line for different values of surface tension gradient overlaid in red on experimental case 400mm/sec 125W.

3.2.6. Single Pass

Single pass models of the parameters found in Table 4 **Error! Reference source not found.** for experiments were performed with and without fluid flow accounted for. The hardness profiles of the no flow and flow cases are shown in Figure 31 and Figure 32 respectively. The first thing to notice is the large difference in shape by simply including the liquid flow dominated by the surface tension gradient. The dimensions related to maximum hardness and maximum hardness of all modeled single pass cases are given in Table 9 for easier discussion of comparison. The reason for focusing on the dimensions of the higher hardness regions instead of the melt line is explained by looking at the solidification line overlaid on the predicted martensitic transformation in Figure 33. In all cases the transformation of martensite exceeds the melt line between 5-10 μm . When the hardness profile is overlaid on an experimental case as in Figure 34 there shows very good agreement lending further support that there is a region that is transformed to austenite outside of

the melt pool and also quickly quenches to martensite. But there is still the slightly hardened region that is beyond the fully hard region. This corresponds to the partially transformed region shown in Figure 18 where the pearlite had enough time for carbon diffusion and transformation to austenite while the ferrite did not as proposed by Orazi et al.[18] Based on the rapid cooling of the single pass and the low final temperature as shown in Figure 23 tempering is not expected to occur.

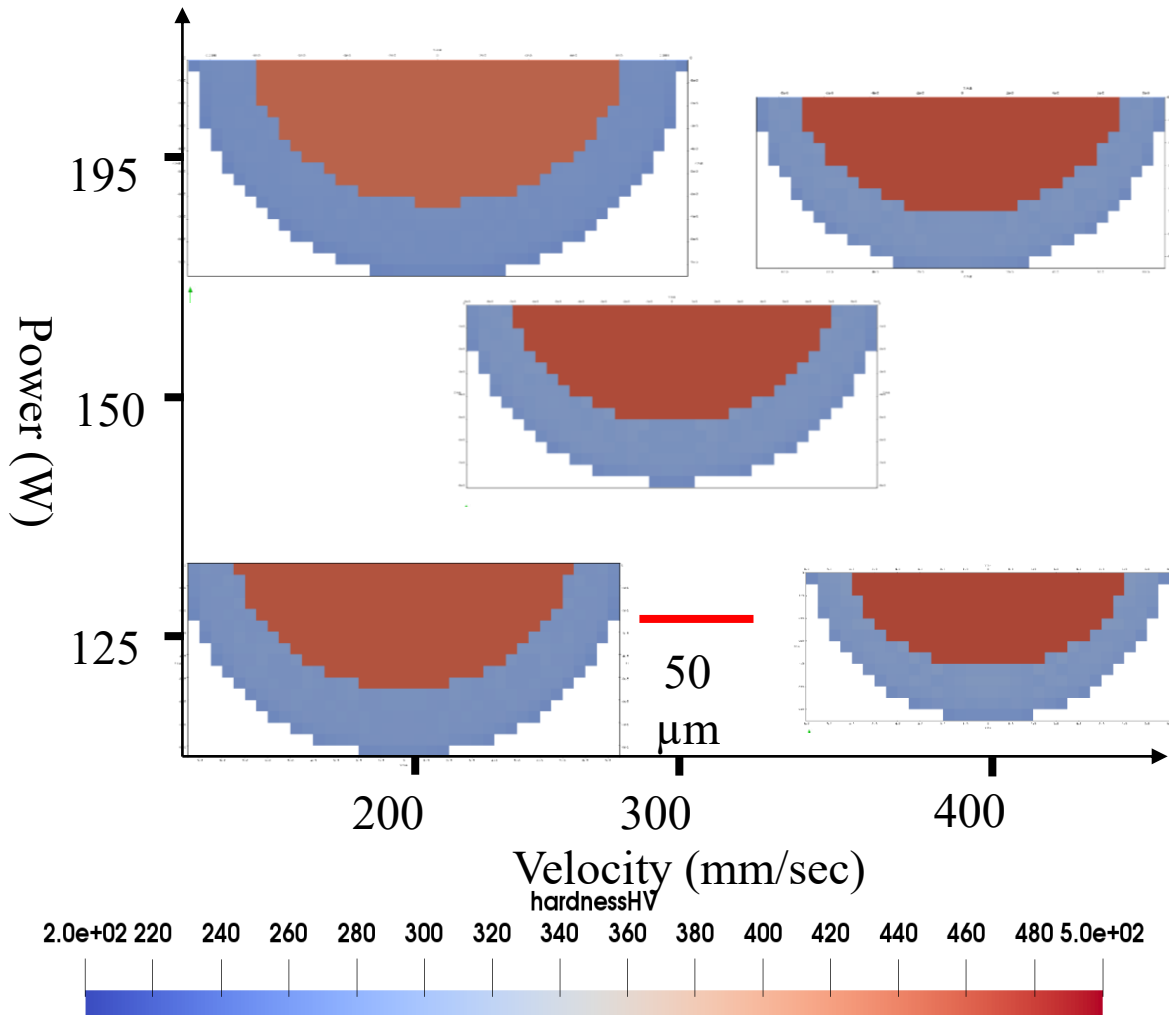


Figure 31: Single Pass no flow model cases depicting hardness.

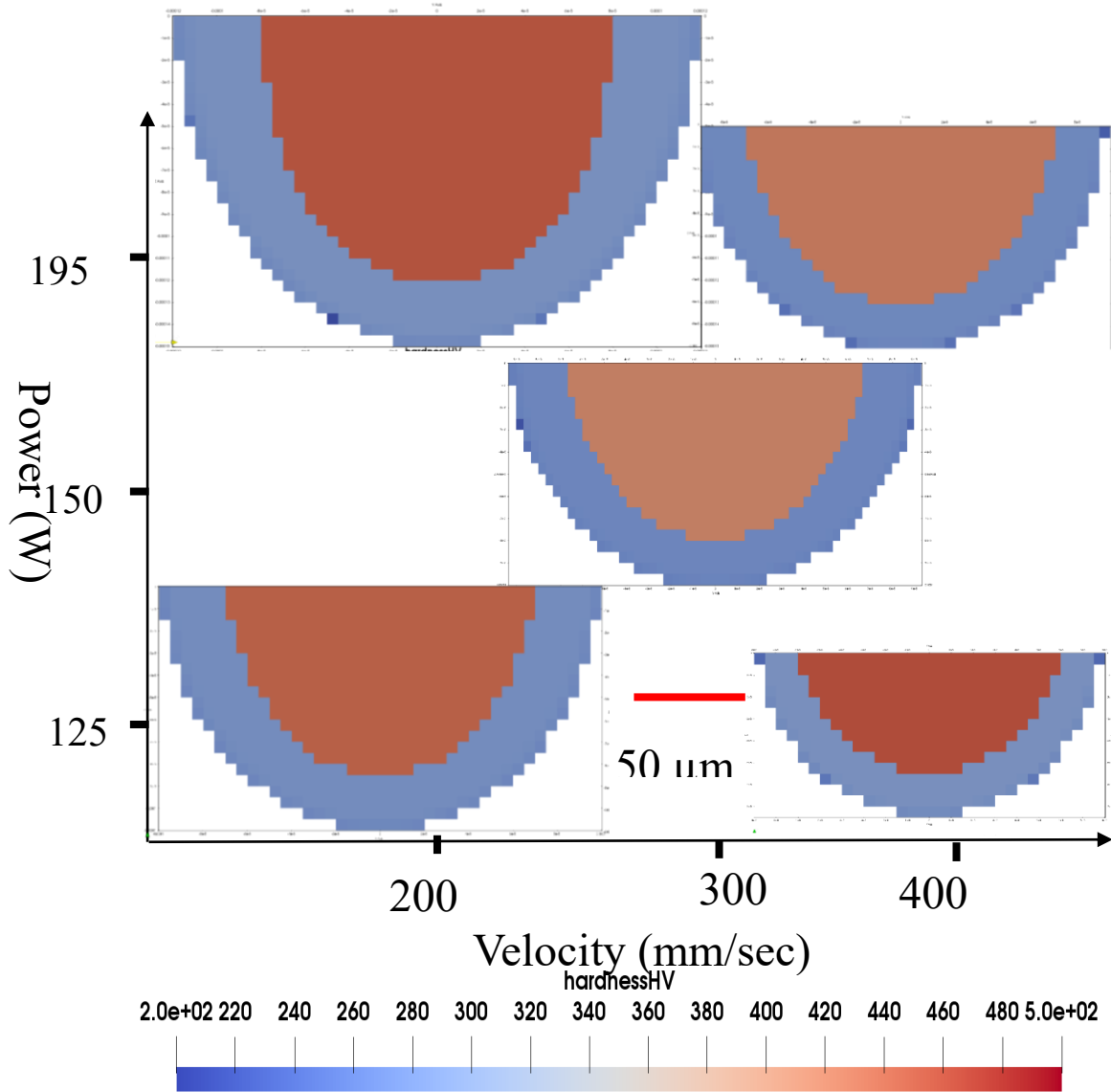


Figure 32: Single pass flow model cases depicting hardness.

Table 9: Compiled dimensions and hardness predictions of single pass cases.

Speed (mm/sec)	Power (W)	No Flow		Flow	
		Hardened Dimensions:	Max Hardness (HV)	Dimensions: width x depth (μm)	Hardness (HV)

		width x depth (μm)			
400	195	140x50	431	140x80	463
400	125	120x40	460	120x55	465
300	150	140x50	417	130x80	462
200	195	160x65	457	160x120	441
200	125	150x55	451	140x85	455

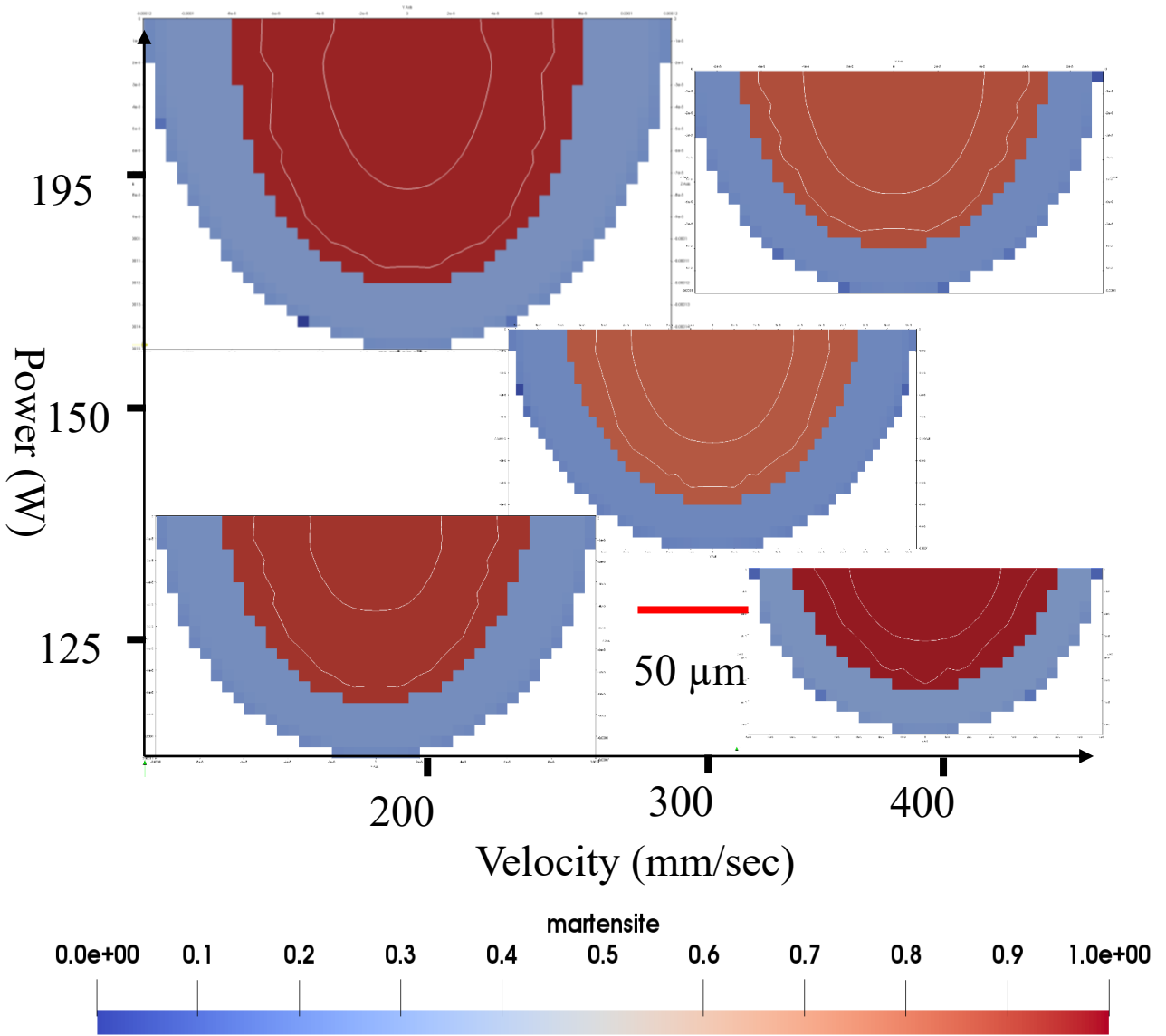


Figure 33: Predicted martensite fraction of single pass weld pools with flow with size of the melt pool overlaid as the larger radial white contour.

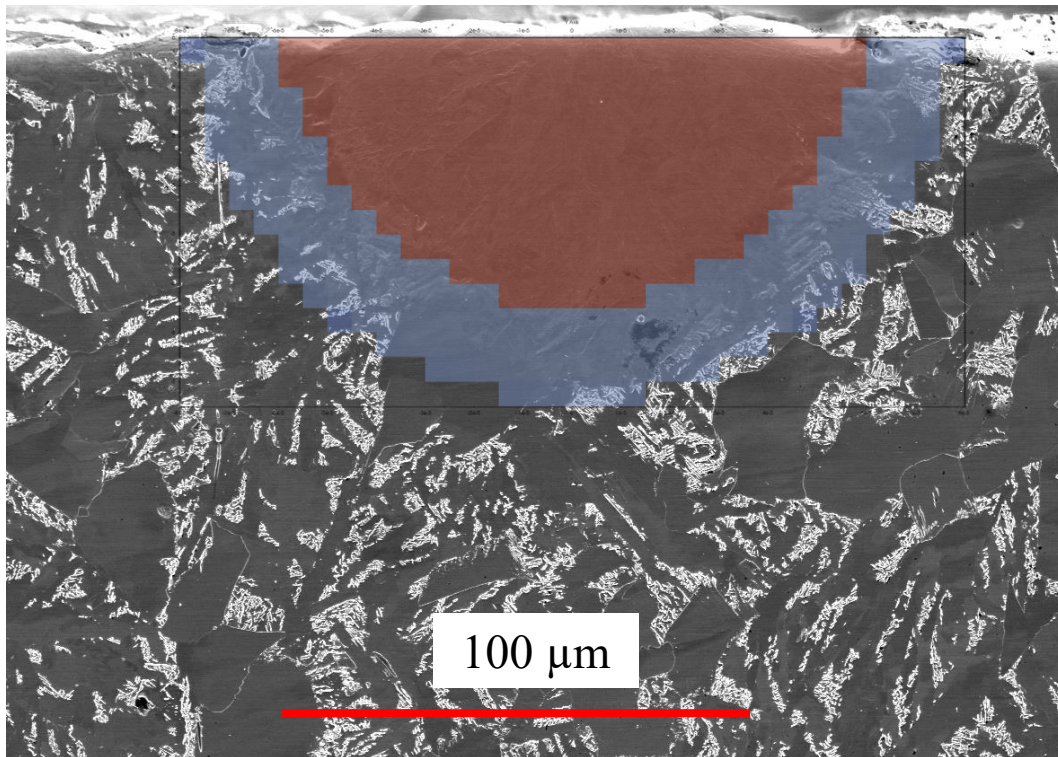


Figure 34: Hardness prediction overlaid on experimental case for 400mm/sec 125W.

3.2.7. Multi-Pass

Multiple pass models of the parameters found in Table 4 for experiments were performed solely without fluid flow accounted for. The multi-pass cases consisted of ten laser passes hatching back and forth each pass. The large number of passes was to ensure a steady state was reached in the middle passes to simulate a large layer being processed. The middle passes' hardness predictions are shown in Figure 35 for all cases. These cases have the earliest laser pass on the left side and progress to the right. Based on Figure 24, tempering is expected to occur due to the rapid heating of subsequent passes. While the total time at temperature is low, since the temperature can reach close to austenitization temperatures diffusion can occur enough to allow for appreciable tempering. The maximum hardness of the multi-pass phases can be found in Table 10 where the maximum hardness appears to have slightly decreased from the single passes with a considerable drop in the overlapped regions. These values also appear to match more closely with the experimental hardness of the multi-pass cases measured in the tempered region and high energy case of 200mm/sec and 195W.

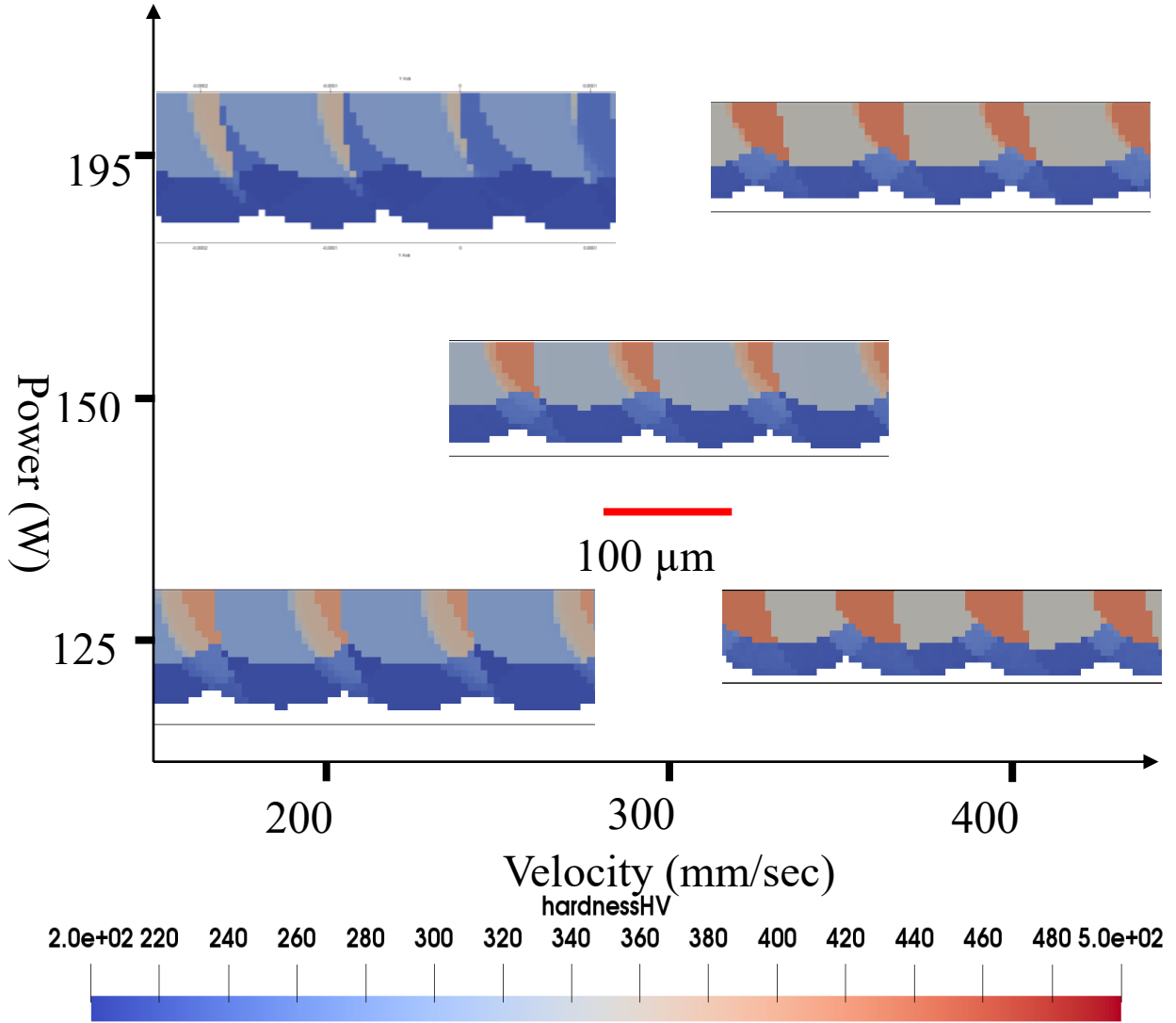


Figure 35: Predicted hardness profiles of multi-pass cases.

Table 10: Maximum hardness predicted for each multi-pass case.

Speed (mm/sec)	Power (W)	Unaffected zone Hardness (HV)	Tempered zone Hardness (HV)
400	195	433	348
400	125	433	349
300	150	424	325
200	195	407	288
200	125	407	288

4. SUMMARY AND FUTURE WORK

This study was able to match weld pools within the conduction regime and was able to explain variations in pools where fluid flow dominated.[10] Phase fraction calculations based on the equations provided by Fortunato et al was shown to be reasonably accurate for laser melting.[34] Hardness predictions based on the thermal history and phase fractions were lower than experimental values but were more in line with what was expected based on the Jominy End Quench tests performed for AISI 8620.[49] Etchants were shown to play a large role in what information can be gathered from the samples. Most people who reported etching only reported one etchant and very few reported information about choice of etchant. While it is understandable that superalloys may be difficult to etch, multiple groups investigating steels used differing etchants without explanation as to why. Only Wang et al gave a reason for their etchant but then later had to use a scanning electron microscope for grain analysis as the etchant did not allow visualization of desired grain structures.[4] While it is not new information that different etchants have different effects on a material, it may be worth exploring how various etchants react to reveal different parts of the microstructure in AM.

Future work would include expanding the experimental space to ensure that there is true matching throughout the no-flow dominated regime and to provide statistical evidence of accuracy of data. Investigation of adding new layers of material would be ideal to see the evolution of the cases as previously melted areas are remelted and processed. This would allow discussion and prediction into a full part build if the data could be matched experimentally. More thorough hardness investigations could potentially yield more understanding of the reported mismatch between the hardness of the samples versus what is expected from the model and the Jominy end quench. Martensite hardness calculations are supposed to already consider lattice distortions caused by dislocations but as of yet there is no other explanation for the difference in hardness.

REFERENCES

- [1] A. S. Wu, D. W. Brown, M. Kumar, G. F. Gallegos, and W. E. King, “An Experimental Investigation into Additive Manufacturing-Induced Residual Stresses in 316L Stainless Steel,” *Metall. Mater. Trans. A Phys. Metall. Mater. Sci.*, vol. 45, no. 13, pp. 6260–6270, Oct. 2014, doi: 10.1007/s11661-014-2549-x.
- [2] K. Shah, A. J. Pinkerton, A. Salman, and L. Li, “Effects of Melt Pool Variables and Process Parameters in Laser Direct Metal Deposition of Aerospace Alloys,” *Mater. Manuf. Process.*, vol. 25, no. 12, pp. 1372–1380, Dec. 2010, doi: 10.1080/10426914.2010.480999.
- [3] L. Sheridan, O. E. Scott-Emuakpor, T. George, and J. E. Gockel, “Relating porosity to fatigue failure in additively manufactured alloy 718,” *Mater. Sci. Eng. A*, vol. 727, pp. 170–176, Jun. 2018, doi: 10.1016/j.msea.2018.04.075.
- [4] Z. Wang, T. A. Palmer, and A. M. Beese, “Effect of processing parameters on microstructure and tensile properties of austenitic stainless steel 304L made by directed energy deposition additive manufacturing,” *Acta Mater.*, vol. 110, pp. 226–235, May 2016, doi: 10.1016/j.actamat.2016.03.019.
- [5] S. Dadbakhsh, L. Hao, and N. Sewell, “Effect of selective laser melting layout on the quality of stainless steel parts,” *Rapid Prototyp. J.*, vol. 18, no. 3, pp. 241–249, 2012, doi: 10.1108/13552541211218216.
- [6] M. Averyanova, P. Bertrand, and B. Verquin, “Studying the influence of initial powder characteristics on the properties of final parts manufactured by the selective laser melting technology,” *Virtual Phys. Prototyp.*, vol. 6, no. 4, pp. 215–223, Dec. 2011, doi: 10.1080/17452759.2011.594645.
- [7] Y. Liu, Y. Yang, S. Mai, D. Wang, and C. Song, “Investigation into spatter behavior during selective laser melting of AISI 316L stainless steel powder,” *Mater. Des.*, vol. 87, pp. 797–806, Dec. 2015, doi: 10.1016/j.matdes.2015.08.086.
- [8] I. A. Roberts, C. J. Wang, R. Esterlein, M. Stanford, and D. J. Mynors, “A three-dimensional finite element analysis of the temperature field during laser melting of metal powders in additive layer manufacturing,” *Int. J. Mach. Tools Manuf.*, vol. 49, no. 12–13, pp. 916–923, Oct. 2009, doi: 10.1016/j.ijmachtools.2009.07.004.

- [9] S. Ly, A. M. Rubenchik, S. A. Khairallah, G. Guss, and M. J. Matthews, “Metal vapor micro-jet controls material redistribution in laser powder bed fusion additive manufacturing,” *Sci. Rep.*, vol. 7, no. 1, pp. 1–12, Dec. 2017, doi: 10.1038/s41598-017-04237-z.
- [10] J. Coleman *et al.*, “Sensitivity of Thermal Predictions to Uncertain Surface Tension Data in Laser Additive Manufacturing,” *In Review*. 2020.
- [11] L. E. Criales, Y. M. Arısoy, B. Lane, S. Moylan, A. Donmez, and T. Özel, “Predictive modeling and optimization of multi-track processing for laser powder bed fusion of nickel alloy 625,” *Addit. Manuf.*, vol. 13, pp. 14–36, Jan. 2017, doi: 10.1016/j.addma.2016.11.004.
- [12] L. Wang and S. Felicelli, “Process modeling in laser deposition of multilayer SS410 steel,” *J. Manuf. Sci. Eng. Trans. ASME*, vol. 129, no. 6, pp. 1028–1034, Dec. 2007, doi: 10.1115/1.2738962.
- [13] A. R. Nassar, M. A. Gundermann, E. W. Reutzler, P. Guerrier, M. H. Krane, and M. J. Weldon, “Formation processes for large ejecta and interactions with melt pool formation in powder bed fusion additive manufacturing,” *Sci. Rep.*, vol. 9, no. 1, pp. 1–11, Dec. 2019, doi: 10.1038/s41598-019-41415-7.
- [14] S. A. Khairallah, A. T. Anderson, A. Rubenchik, and W. E. King, “Laser powder-bed fusion additive manufacturing: Physics of complex melt flow and formation mechanisms of pores, spatter, and denudation zones,” *Acta Mater.*, vol. 108, pp. 36–45, Apr. 2016, doi: 10.1016/j.actamat.2016.02.014.
- [15] W. E. Frazier, “Metal additive manufacturing: A review,” *Journal of Materials Engineering and Performance*, vol. 23, no. 6. Springer New York LLC, pp. 1917–1928, 08-Apr-2014, doi: 10.1007/s11665-014-0958-z.
- [16] Y. Kawahito, M. Mizutani, and S. Katayama, “High quality welding of stainless steel with 10 kW high power fibre laser,” *Sci. Technol. Weld. Join.*, vol. 14, no. 4, pp. 288–294, May 2009, doi: 10.1179/136217108X372531.
- [17] R. S. Lakhkar, Y. C. Shin, and M. J. M. Krane, “Predictive modeling of multi-track laser hardening of AISI 4140 steel,” *Mater. Sci. Eng. A*, vol. 480, no. 1–2, pp. 209–217, May 2008, doi: 10.1016/j.msea.2007.07.054.

- [18] L. Orazi, A. Fortunato, G. Tani, G. Campana, A. Ascari, and G. Cuccolini, "A new computationally efficient method in laser hardening modeling," in *Proceedings of the ASME International Manufacturing Science and Engineering Conference, MSEC2008*, 2009, vol. 1, pp. 211–218, doi: 10.1115/MSEC_ICMP2008-72501.
- [19] C. P. Paul, H. Alemohammad, E. Toyserkani, A. Khajepour, and S. Corbin, "Cladding of WC-12 Co on low carbon steel using a pulsed Nd:YAG laser," *Mater. Sci. Eng. A*, vol. 464, no. 1–2, pp. 170–176, Aug. 2007, doi: 10.1016/j.msea.2007.01.132.
- [20] D. Zhang, Z. Feng, C. Wang, W. Wang, Z. Liu, and W. Niu, "Comparison of microstructures and mechanical properties of Inconel 718 alloy processed by selective laser melting and casting," *Mater. Sci. Eng. A*, vol. 724, pp. 357–367, May 2018, doi: 10.1016/j.msea.2018.03.073.
- [21] S. S. Babu, "Science and Technology of Welding and Joining In pursuit of optimum welding system design for steels In pursuit of optimum welding system design for steels," doi: 10.1179/1362171811Y.0000000019.
- [22] S. Vignier, E. Biro, and M. Hervé, "Predicting the hardness profile across resistance spot welds in martensitic steels," doi: 10.1007/s40194-014-0116-0.
- [23] X. L. Gao, L. J. Zhang, J. Liu, and J. X. Zhang, "A comparative study of pulsed Nd: YAG laser welding and TIG welding of thin Ti6Al4V titanium alloy plate," *Mater. Sci. Eng. A*, vol. 559, pp. 14–21, Jan. 2013, doi: 10.1016/j.msea.2012.06.016.
- [24] E. Akman, A. Demir, T. Canel, and T. Sinmazçelik, "Laser welding of Ti6Al4V titanium alloys," *J. Mater. Process. Technol.*, vol. 209, no. 8, pp. 3705–3713, Apr. 2009, doi: 10.1016/j.jmatprotec.2008.08.026.
- [25] H. Wang, Y. Zhang, and K. Chen, "Modeling of Temperature Distribution in Laser Welding of Lapped Martensitic Steel M1500 and Softening Estimation," 2016, doi: 10.1115/1.4033391.
- [26] B. J. Keene, K. C. Mills, and R. F. Brooks, "Surface properties of liquid metals and their effects on weldability," *Mater. Sci. Technol. (United Kingdom)*, vol. 1, no. 7, pp. 559–567, 1985, doi: 10.1179/mst.1985.1.7.559.
- [27] Z. S. Saldi, "Marangoni driven free surface flows in liquid weld pools," 2011.

- [28] F. Weng, C. Chen, and H. Yu, "Research status of laser cladding on titanium and its alloys: A review," *Materials and Design*, vol. 58. Elsevier Ltd, pp. 412–425, 01-Jun-2014, doi: 10.1016/j.matdes.2014.01.077.
- [29] A. Frenk, M. Vandyoussefi, J.-D. Wagnie`re, W. Wagnie`re, A. Zryd, and W. Kurz, "Analysis of the Laser-Cladding Process for Stellite on Steel," 1997.
- [30] Q. Ming, L. C. Lim, and Z. D. Chen, "Laser cladding of nickel-based hardfacing alloys," *Surf. Coatings Technol.*, vol. 106, no. 2–3, pp. 174–182, Aug. 1998, doi: 10.1016/S0257-8972(98)00524-6.
- [31] J. M. Yellup, "Laser cladding using the powder blowing technique," *Surf. Coatings Technol.*, vol. 71, no. 2, pp. 121–128, Mar. 1995, doi: 10.1016/0257-8972(94)01010-G.
- [32] L. Giorleo, B. Previtali, and Q. Semeraro, "Modelling of back tempering in laser hardening," *Int. J. Adv. Manuf. Technol.*, vol. 54, no. 9–12, pp. 969–977, 2011, doi: 10.1007/s00170-010-3008-5.
- [33] A. Fortunato, L. Orazi, G. Cuccolini, and A. Ascari, "An exhaustive model for the laser hardening of hypo eutectoid steel," *High-Power Laser Mater. Process. Lasers, Beam Deliv. Diagnostics, Appl. II*, vol. 8603, no. February 2013, p. 86030F, 2013, doi: 10.1117/12.2007389.
- [34] A. Fortunato, L. Orazi, and G. Tani, "A new computationally efficient model for tempering in multitrack laser hardening in medium carbon steels," *J. Manuf. Sci. Eng. Trans. ASME*, vol. 133, no. 2, Apr. 2011, doi: 10.1115/1.4003522.
- [35] H. Gong, K. Rafi, H. Gu, T. Starr, and B. Stucker, "Analysis of defect generation in Ti-6Al-4V parts made using powder bed fusion additive manufacturing processes," *Addit. Manuf.*, vol. 1, pp. 87–98, Oct. 2014, doi: 10.1016/j.addma.2014.08.002.
- [36] G. E. Bean, D. B. Witkin, T. D. McLouth, D. N. Patel, and R. J. Zaldivar, "Effect of laser focus shift on surface quality and density of Inconel 718 parts produced via selective laser melting," *Addit. Manuf.*, vol. 22, pp. 207–215, Aug. 2018, doi: 10.1016/j.addma.2018.04.024.
- [37] S. Pang, X. Chen, J. Zhou, X. Shao, and C. Wang, "3D transient multiphase model for keyhole, vapor plume, and weld pool dynamics in laser welding including the ambient pressure effect," *Opt. Lasers Eng.*, vol. 74, pp. 47–58, May 2015, doi: 10.1016/j.optlaseng.2015.05.003.

- [38] P. Bidare, I. Bitharas, R. M. Ward, M. M. Attallah, and A. J. Moore, “Laser powder bed fusion in high-pressure atmospheres,” *Int. J. Adv. Manuf. Technol.*, vol. 99, no. 1–4, pp. 543–555, Aug. 2018, doi: 10.1007/s00170-018-2495-7.
- [39] P. Bidare, I. Bitharas, R. M. Ward, M. M. Attallah, and A. J. Moore, “Laser powder bed fusion at sub-atmospheric pressures,” *Int. J. Mach. Tools Manuf.*, vol. 130–131, pp. 65–72, Aug. 2018, doi: 10.1016/j.ijmactools.2018.03.007.
- [40] B. Liu, R. Wildman, C. Tuck, I. Ashcroft, and R. Hague, “INVESTIGATION THE EFFECT OF PARTICLE SIZE DISTRIBUTION ON PROCESSING PARAMETERS OPTIMISATION IN SELECTIVE LASER MELTING PROCESS.”
- [41] H. P. Tang, M. Qian, N. Liu, X. Z. Zhang, G. Y. Yang, and J. Wang, “Effect of Powder Reuse Times on Additive Manufacturing of Ti-6Al-4V by Selective Electron Beam Melting,” *JOM*, vol. 67, no. 3, pp. 555–563, Feb. 2015, doi: 10.1007/s11837-015-1300-4.
- [42] W. King, A. T. Anderson, R. M. Ferencz, N. E. Hodge, C. Kamath, and S. A. Khairallah, “Overview of modelling and simulation of metal powder bed fusion process at Lawrence Livermore National Laboratory,” *Mater. Sci. Technol.*, vol. 31, no. 8, pp. 957–968, Jun. 2015, doi: 10.1179/1743284714Y.00000000728.
- [43] W. E. King *et al.*, “Laser powder bed fusion additive manufacturing of metals; physics, computational, and materials challenges,” *Appl. Phys. Rev.*, vol. 2, no. 4, p. 041304, Dec. 2015, doi: 10.1063/1.4937809.
- [44] T. Mukherjee, H. L. Wei, A. De, and T. DebRoy, “Heat and fluid flow in additive manufacturing – Part II: Powder bed fusion of stainless steel, and titanium, nickel and aluminum base alloys,” *Comput. Mater. Sci.*, 2018, doi: 10.1016/j.commatsci.2018.04.027.
- [45] L. Costa, R. Vilar, T. Reti, and A. M. Deus, “Rapid tooling by laser powder deposition: Process simulation using finite element analysis,” *Acta Mater.*, vol. 53, no. 14, pp. 3987–3999, Aug. 2005, doi: 10.1016/j.actamat.2005.05.003.
- [46] D. P. Townsend, “Surface Fatigue Life and Failure Characteristics of EX-53, CBS 1000M, and AISI 9310 Gear Materials,” Oct. 1985.
- [47] Y. Xiao, “Effect of laser shock peening on bending fatigue performance of AISI 9310 steel spur gear,” *Opt. Laser Technol.*, vol. 94, pp. 15–24, Sep. 2017, doi: 10.1016/j.optlastec.2017.03.017.

- [48] D. P. Townsend, J. J. Coy, and E. V. Zaretsky, "Experimental and analytical load-life relation for AISI 9310 steel spur gears," *J. Mech. Des. Trans. ASME*, vol. 100, no. 1, pp. 54–60, Jan. 1978, doi: 10.1115/1.3453893.
- [49] G. F. V. Voort, *Atlas of Time-Temperature Diagrams*. 1991.
- [50] G. F. Vander Voort, "Phase Identification by Selective Etching," in *Applied Metallography*, Springer US, 1986, pp. 1–19.
- [51] K. Moussaoui, W. Rubio, M. Mousseigne, T. Sultan, and F. Rezai, "Effects of Selective Laser Melting additive manufacturing parameters of Inconel 718 on porosity, microstructure and mechanical properties," *Mater. Sci. Eng. A*, vol. 735, pp. 182–190, Sep. 2018, doi: 10.1016/j.msea.2018.08.037.
- [52] X. Zhao, J. Chen, X. Lin, and W. Huang, "Study on microstructure and mechanical properties of laser rapid forming Inconel 718," *Mater. Sci. Eng. A*, vol. 478, no. 1–2, pp. 119–124, Apr. 2008, doi: 10.1016/j.msea.2007.05.079.
- [53] T. Trosch, J. Strößner, R. Völkl, and U. Glatzel, "Microstructure and mechanical properties of selective laser melted Inconel 718 compared to forging and casting," *Materials Letters*, vol. 164. Elsevier B.V., pp. 428–431, 01-Feb-2016, doi: 10.1016/j.matlet.2015.10.136.
- [54] D. Zhang, W. Niu, X. Cao, and Z. Liu, "Effect of standard heat treatment on the microstructure and mechanical properties of selective laser melting manufactured Inconel 718 superalloy," *Mater. Sci. Eng. A*, vol. 644, pp. 32–40, Sep. 2015, doi: 10.1016/j.msea.2015.06.021.
- [55] T. L. Starr, K. Rafi, B. Stucker, and C. M. Scherzer, "CONTROLLING PHASE COMPOSITION IN SELECTIVE LASER MELTED STAINLESS STEELS."
- [56] A. Yadollahi, N. Shamsaei, S. M. Thompson, A. Elwany, and L. Bian, "Effects of building orientation and heat treatment on fatigue behavior of selective laser melted 17-4 PH stainless steel," *Int. J. Fatigue*, vol. 94, pp. 218–235, Jan. 2017, doi: 10.1016/j.ijfatigue.2016.03.014.
- [57] L. Caprio, A. G. Demir, and B. Previtali, "Influence of pulsed and continuous wave emission on melting efficiency in selective laser melting," *J. Mater. Process. Technol.*, vol. 266, pp. 429–441, Apr. 2019, doi: 10.1016/j.jmatprotec.2018.11.019.

- [58] V. D. Manvatkar, A. A. Gokhale, G. J. Reddy, U. Savitha, and A. De, “Investigation on laser engineered net shaping of multilayered structures in H13 tool steel,” *J. Laser Appl.*, vol. 27, no. 3, p. 032010, Aug. 2015, doi: 10.2351/1.4921493.
- [59] X. Lin, Y. Cao, X. Wu, H. Yang, J. Chen, and W. Huang, “Microstructure and mechanical properties of laser forming repaired 17-4PH stainless steel,” *Mater. Sci. Eng. A*, vol. 553, pp. 80–88, Sep. 2012, doi: 10.1016/j.msea.2012.05.095.
- [60] L. E. Murr *et al.*, “Microstructures and properties of 17-4 PH stainless steel fabricated by selective laser melting,” *J. Mater. Res. Technol.*, vol. 1, no. 3, pp. 167–177, Oct. 2012, doi: 10.1016/S2238-7854(12)70029-7.
- [61] A. B. Spierings and G. Levy, “Comparison of density of stainless steel 316L parts produced with selective laser melting using different powder grades.”
- [62] I. Yadroitsev and I. Smurov, “Selective laser melting technology: From the single laser melted track stability to 3D parts of complex shape,” in *Physics Procedia*, 2010, vol. 5, no. PART 2, pp. 551–560, doi: 10.1016/j.phpro.2010.08.083.
- [63] A. Laohaprapanon *et al.*, “Optimal Scanning Condition of Selective Laser Melting Processing with Stainless Steel 316L Powder,” 2012, doi: 10.4028/www.scientific.net/AMR.341-342.816.
- [64] C. Kamath, B. El-Dasher, G. F. Gallegos, W. E. King, and A. Sisto, “Density of additively-manufactured, 316L SS parts using laser powder-bed fusion at powers up to 400 W,” *Int. J. Adv. Manuf. Technol.*, vol. 74, no. 1–4, pp. 65–78, May 2014, doi: 10.1007/s00170-014-5954-9.
- [65] J. Davis, K. Mills, and S. Lampman, “Metals Handbook. Tenth Edition. Vol. 1. Properties and Selection: Irons, Steels, and High-Performance Alloys,” *ASM Int. Mater. Park. Ohio 44073, USA, 1990. 1063 pp*, p. 1063.
- [66] U. S. D. of Defense, “Standard Test Methods for Vickers Hardness and Knoop Hardness of Metallic Materials,” doi: 10.1520/E0092-17.
- [67] D. Hömberg, “A numerical simulation of the Jominy end-quench test,” *Acta Mater.*, 1996, doi: 10.1016/1359-6454(96)00084-5.
- [68] N. I. Kobasko, “Steel Superstrengthening Phenomenon,” 2005.

- [69] E. OHMURA, K. INOUE, and K. HARUTA, “Computer Simulation on Structural Changes of Hypoeutectoid Steel in Laser Transformation Hardening Process,” *JSME Int. journal. Ser. 1, Solid Mech. strength Mater.*, vol. 32, no. 1, pp. 45–53, Jan. 1989, doi: 10.1299/jsmea1988.32.1_45.
- [70] S. M. C. Van Bohemen and J. Sietsma, “Effect of composition on kinetics of athermal martensite formation in plain carbon steels,” *Mater. Sci. Technol.*, vol. 25, no. 8, pp. 1009–1012, Aug. 2009, doi: 10.1179/174328408X365838.
- [71] G. F. Vander Voort, *Applied Metallography*. Springer US, 1986.
- [72] S. Kou, *Welding metallurgy*, 2nd ed. Hoboken, N.J.: Wiley-Interscience, 2003.
- [73] P. K. Sung, D. R. Poirier, and S. D. Felicelli, “Modelling and Simulation in Materials Science and Engineering Continuum model for predicting microporosity in steel castings Continuum model for predicting microporosity in steel,” 2002.
- [74] A. J. Pinkerton and L. Li, “An analytical model of energy distribution in laser direct metal deposition,” *Proc. Inst. Mech. Eng. Part B J. Eng. Manuf.*, vol. 218, no. 4, pp. 363–374, Apr. 2004, doi: 10.1243/095440504323055498.
- [75] M. Avrami, “Kinetics of phase change. II Transformation-time relations for random distribution of nuclei,” *J. Chem. Phys.*, vol. 8, no. 2, pp. 212–224, Feb. 1940, doi: 10.1063/1.1750631.
- [76] J. Rohde and A. Jeppsson, “Literature review of heat treatment simulations with respect to phase transformation, residual stresses and distortion,” *Scand. J. Metall.*, vol. 29, no. 2, pp. 47–62, 2000, doi: 10.1034/j.1600-0692.2000.d01-6.x.
- [77] C. Şimşir and C. H. Gür, “A FEM based framework for simulation of thermal treatments: Application to steel quenching,” *Comput. Mater. Sci.*, vol. 44, no. 2, pp. 588–600, Dec. 2008, doi: 10.1016/j.commatsci.2008.04.021.
- [78] D. P. Koistinen and R. E. Marburger, “A general equation prescribing the extent of the austenite-martensite transformation in pure iron-carbon alloys and plain carbon steels,” *Acta Metallurgica*, vol. 7, no. 1. Pergamon, pp. 59–60, 01-Jan-1959, doi: 10.1016/0001-6160(59)90170-1.
- [79] A. Fortunato, A. Ascari, E. Liverani, L. Orazi, and G. Cuccolini, “A comprehensive model for laser hardening of carbon steels,” *J. Manuf. Sci. Eng. Trans. ASME*, vol. 135, no. 6, Dec. 2013, doi: 10.1115/1.4025563.

- [80] L. Orazi, A. Fortunato, G. Cuccolini, and G. Tani, “An efficient model for laser surface hardening of hypo-eutectoid steels,” *Appl. Surf. Sci.*, vol. 256, no. 6, pp. 1913–1919, Jan. 2010, doi: 10.1016/j.apsusc.2009.10.037.
- [81] Asm International, “Heat Treating, Vol. 4,” *ASM Int. Mater. Park. OH*, p. 860, 1991.